Global climate modelling of Saturn's atmosphere, Part V: Large-scale vortices

Padraig T Donnelly, Aymeric Spiga, Sandrine Guerlet, Matt K James, Deborah Bardet

Icarus 425 (2025) 116302

Contents lists available at ScienceDirect

Icarus

journal homepage: www.elsevier.com/locate/icarus

Research Paper

Global climate modelling of Saturn's atmosphere, Part V: Large-scale vortices

Padraig T. Donnelly [a,b,*], Aymeric Spiga [b,c], Sandrine Guerlet [b,d], Matt K. James [e], Deborah Bardet [b]

[a] DMPE, ONERA, Université Paris-Saclay, F-91123 Palaiseau, France
[b] Laboratoire de Météorologie Dynamique/Institut Pierre-Simon Laplace (LMD/IPSL), Sorbonne Université, Centre National de la Recherche Scientifique (CNRS), École Polytechnique, École Normale Supérieure (ENS), Campus Pierre et Marie Curie BC99, 4 place Jussieu, 75005 Paris, France
[c] Institut Universitaire de France (IUF), 1 rue Descartes, 75005 Paris, France
[d] LESIA, Observatoire de Paris, Université PSL, CNRS, Sorbonne Université, Univ. Paris Diderot, Sorbonne Paris Cité, 5 place Jules Janssen, 92195 Meudon, France
[e] University of Leicester, University of Leicester, University Road, Leicester, LE1 7RH, UK

ARTICLE INFO

Dataset link: https://github.com/PTDonnelly/dynamico_gcm

Keywords:
Gas giants
Saturn
Vortices
Global climate model
Eddy-to-mean flow interactions
Geospatial information systems
Machine learning
Dynamical detection
Atmospheric dynamics

ABSTRACT

This paper presents an analysis of large-scale vortices in the atmospheres of gas giants, focusing on a detailed study conducted using the Saturn-DYNAMICO global climate model (GCM). Large-scale vortices, a prominent feature of gas giant atmospheres, play a critical role in their atmospheric dynamics. By employing three distinct methods – manual detection, machine learning via artificial neural networks (ANN), and dynamical detection using the Automated Eddy-Detection Algorithm (AMEDA) – we characterise the spatial, temporal, and dynamical properties of these vortices within the Saturn-DYNAMICO GCM. Our findings reveal a consistent production of vortices due to well-resolved eddy-to-mean flow interactions, exhibiting size and intensity distributions broadly in agreement with observational data. However, notable differences in vortex location, size, and concentration highlight the model's limitations and suggest areas for further refinement. The analysis underscores the importance of zonal wind conditions in influencing vortex characteristics and suggests that more accurate modelling of giant planet vortices may require improved representation of moist convection and jet structure. This study not only provides insights into the dynamics of Saturn's atmosphere as simulated by the GCM but also offers a framework for comparing vortex characteristics across observations and models of planetary atmospheres.

1. Introduction

A general feature of planetary atmospheres is the presence of strong zonal flows that arise from thermal gradients and planetary rotation effects. The complex interaction between eddy momentum fluxes and these zonal jets can often give rise to intense shears and retrograde flows which can lead to vortical structures. These dynamically-closed features are found in many planetary atmospheres.

Vortices are ubiquitous on Jupiter, with a great deal of variability in spatial structure and lifetime between the largely cool and cloudy white anticyclones to the warm and volatile-rich dark cyclones (Smith et al., 1979; Ingersoll et al., 1979; Mitchell et al., 1979; Rogers, 1995; Vasavada et al., 1998; Fletcher et al., 2022; Orton et al., 2022). Jovian anticyclones are often more long-lived than their cyclonic counterparts, sometimes existing for many years, compared to the often transient cyclones. Cyclones are generally fewer in number and potentially far more irregular in shape, sometimes being quite zonally-oblate (Morales-Juberìas et al., 2002; Legarreta and Sánchez-Lavega, 2005). Jovian cyclones and anticyclones typically form in their associated region of shear with vorticity magnitudes on the order of the planetary and local wind shear vorticities (Mac Low and Ingersoll, 1986; Legarreta and Sánchez-Lavega, 2005). Recent observations from the NASA Juno spacecraft reveal complex, stable configurations of circumpolar cyclones, of a kind that are not observed on other giant planets (Orton et al., 2017; Adriani et al., 2018).

The atmosphere of Saturn exhibits fewer discrete vortices than Jupiter. Prominent anticyclonic white ovals have been observed from the Pic-du-Midi Observatory (Sánchez-Lavega et al., 1997), and by the Voyager (Smith et al., 1981, 1982; García-Melendo et al., 2007) and Cassini (Vasavada et al., 2006; Trammell et al., 2014, 2016) spacecraft, sometimes lasting for years and experiencing merging events with smaller spots. There is a relative dearth of stable cyclonic spots on Saturn, with the most notable being the long-lived and UV-bright spot observed from the ground (Sánchez-Lavega et al., 2000), by Voyager 2 (Smith et al., 1982), and by the Hubble Space Telescope (HST, Caldwell et al., 1993). Cassini also observed the long-lived southern cyclone at ~46°S (del Río-Gaztelurrutia et al., 2010), groups of vortices like the

* Corresponding author.
E-mail address: padraig.donnelly@onera.fr (P.T. Donnelly).

https://doi.org/10.1016/j.icarus.2024.116302
Received 10 April 2024; Received in revised form 3 September 2024; Accepted 4 September 2024
Available online 7 September 2024

relatively long-lived cyclone–anticyclone coupled system at ~59°N (del Río-Gaztelurrutia et al., 2018), the long chain of infrared-bright spots at ~33°N (the "String of Pearls", Sayanagi et al., 2014), and the dark ovals frequently generated in a region of vigorous convection, thunderstorm, and lightning activity at 33–39°N ("Storm Alley" Sromovsky et al., 2018). There has been extensive study of the polar region from ground-based (Orton and Yanamandra-Fisher, 2005) and space-based (Sánchez-Lavega et al., 2006; Dyudina et al., 2008; Fletcher et al., 2008; Dyudina et al., 2009; Baines et al., 2009; Antuñano et al., 2015; Sayanagi et al., 2017; Antuñano et al., 2018) observatories, revealing a circular stable cyclone at each pole. This structure is analogous to the polar cyclones on Jupiter and is expected to be common on the gas giants (O'Neill et al., 2015; Scott, 2011).

On Uranus, ground-based and spacecraft observations (Sromovsky et al., 2012) present a dominant view of clouds exhibiting many small bright spots (potentially regions featuring cumulus-like convection) with associated dark spots. Further ground-based observations (de Pater et al., 2015) detected near-infrared-bright, rapidly-evolving, discrete cloud features that suggest more structured vortical systems deeper in the atmosphere.

On Neptune, the historical record contains two prominent anticyclones imaged by Voyager (Smith et al., 1989; Limaye and Sromovsky, 1991; Sromovsky et al., 1993). Ground-based observations detected a large circumpolar prograde jet at approximately 80°S surrounding an infrared-bright polar region (Luszcz-Cook et al., 2010). These highest southern latitudes exhibit large-scale subsidence, warming, slowing of the peripheral jet, and potential volatile depletion, suggestive of cyclonic motion (Fletcher et al., 2014).

Large-scale vortices are key to understand the atmospheric dynamics on gas giants (Sada et al., 1996; Simon-Miller et al., 2002; Ingersoll et al., 2004; Vasavada and Showman, 2005; del Genio et al., 2009), providing insights into the vertical structure and sources of forcing for long-lived stable features (e.g. zonal jets) and ephemeral convective events (e.g. moist convective outbreaks). Therefore, it is crucial to also consider theoretical models (e.g. radiative, chemical, and dynamical) to enrich knowledge of vortices and large-scale dynamics gained from observations (Ingersoll et al., 1981; Williams and Yamagata, 1984; Dowling and Ingersoll, 1989; Marcus et al., 2000; Li et al., 2006; Showman, 2007; del Río-Gaztelurrutia et al., 2010; Rostami et al., 2017).

In recent years there has been much study into idealised and comprehensive numerical models to investigate large-scale dynamics. A significant challenge in gas giant modelling is representing the depth and forcing of large-scale dynamics. As a result, two approaches have emerged to investigate the tropospheric dynamics on the giant planets. One is the "shallow-forcing" model which uses equations that assume a thin atmosphere to capture weather-layer phenomena like baroclinic instability and moist convective storms (Vasavada and Showman, 2005; Lian and Showman, 2008; Schneider and Liu, 2009; Liu and Schneider, 2010; Lian and Showman, 2010; García-Melendo et al., 2010). The other is the "deep-seated" dynamo-like model that captures convection through the planet's molecular envelope (Heimpel et al., 2005; Yano et al., 2005; Kaspi et al., 2009; Heimpel and Gómez Pérez, 2011; Gastine et al., 2014; Heimpel et al., 2016; Cabanes et al., 2017). The shallow weather-layer models, like the Saturn-DYNAMICO GCM described in this paper, reproduce well convective events, large-scale vortices, and high-latitude westward jets, and the deep-seated models reproduce the strength and stability of the equatorial super-rotating zonal jet, but the challenge remains to capture all of these phenomena under a single scheme (Vasavada and Showman, 2005; Lian and Showman, 2008; Schneider and Liu, 2009; Liu and Schneider, 2010; Lian and Showman, 2010; García-Melendo et al., 2010). However, recent observational studies have shown that jets are much deeper than the vertical extent of shallow-water models, but shallower than what some deep models assume (Kaspi et al., 2018; Guillot et al., 2018; Galanti et al., 2019), implying merits to each methodology for modelling large-scale dynamics.

Despite the many observations of giant planet vortices, it remains a challenge to perform a comprehensive long-term study of the statistical morphologies and dynamics of vortices. Amateur visible-light and near-IR data continues to provide an invaluable scientific tool for vortex classification (Rogers, 1995; Rogers et al., 2006; Iñurrigarro et al., 2020; Hueso et al., 2022), and the NASA Juno spacecraft has enabled unprecedented opportunity to classify the jovian polar and circumpolar vortices (Adriani et al., 2018; Grassi et al., 2018; Kaspi et al., 2018; Adriani et al., 2020; Li et al., 2020; Tabataba-Vakili et al., 2020; Bolton et al., 2021; Scarica et al., 2022; Siegelman et al., 2022a,b). For Saturn, the natural differences in vortex appearance and the relatively lower spatial resolution of amateur observations makes comparable study on Saturn difficult, despite decades of observations from ground-based (Hanel et al., 1981, 1982; Fletcher et al., 2009; Blake et al., 2023) and space-based (Karkoschka and Tomasko, 2005; Pérez-Hoyos et al., 2005; Fletcher et al., 2023) observatories.

Until recently there has not been a fully eddy-resolved, multi-year global circulation model of the gas giants that manifests cloud-top vortices without forcing or parameterisation. The Saturn-DYNAMICO GCM presents a unique opportunity to explore the eddy-driven production of vortices from eddy-jet interaction in the context of a Saturn-like planet (see Section 2). Long-lived, large-scale vortices occur spontaneously in the model, but so far they have not been studied in detail. This work characterises the spatial, temporal, and dynamical structure of these vortices over multiple Saturn years. With the wealth of vortices in the model and the benefits of direct dynamical outputs, we explore three different detection methodologies and compare the results to previous observational studies of vortices on Saturn.

We briefly introduce the reference simulation from Saturn-DYNAMICO GCM in Section 2.1 and the general approach to the detection of large-scale vortices on the giant planets in Section 2.2. In Sections 2.3, 2.4, and 2.5 we introduce the three vortex detection methodologies used in this comparative analysis. Section 3 compares the statistical distributions of model parameters for all vortices detected by the three methods, with a focus on spatial and temporal distributions, vortex size, vortex shape, and local wind conditions. Finally, Section 4 discusses the model vortices in the context of observational studies of the giant planets, reflects on the strengths and limitations of the three methods for vortex detection, and discusses implications for future study.

2. Methodology

2.1. Saturn-DYNAMICO Global Climate Model

The Saturn-DYNAMICO GCM is comprised of a radiative-seasonal model coupled to a hydrodynamical core that solves the shallow-layer equations on an icosahedral grid, with 32 atmospheric layers from 1–3000 mbar (Spiga et al., 2020). The model is optimised for massively-parallel computation which has enabled the high-resolution numerical simulation of Saturn's atmosphere on a half-degree latitude–longitude grid for fifteen modelled planetary years. Radiative transfer modelling uses correlated-k distributions based on HITRAN line data for the primary hydrocarbons (CH_4, C_2H_6, and C_2H_2, Rothman et al., 2013), collision-induced absorption from H_2-H_2, H_2-He, tropospheric and stratospheric aerosols, as well as ring shadowing effects and internal heat fluxes (Guerlet et al., 2014). Along with an internal heat flux, the model has a Rayleigh-like drag layer at the model bottom, which emulates the deep zonal flows and which acts to close the angular momentum budget. Initial winds are set to zero with a single vertical profile of temperature everywhere, and the model has sufficient spatial resolution to directly resolve the eddy-to-mean energy cascade over the long spin-up time of eight years to achieve steady-state flow (Cabanes et al., 2020). This steady state from model year eight to fifteen in Spiga et al. (2020) forms the dataset for this work (discussed in Section 2.2).

The steady-state Saturn-DYNAMICO model produces a thermal structure consistent with Cassini/CIRS measurements of Saturn (Spiga et al., 2020), as well as a realistic zonal jet structure (except for the super-rotating equatorial jet, largely underestimated in the simulation), eddy-acceleration of the jets, and atmospheric planetary-scale waves. Subsequent studies using Saturn-DYNAMICO have explored the inverse cascade giving rise to jets (Cabanes et al., 2020), the stratospheric equatorial dynamics and their impact on the quasi-periodic equatorial oscillation (Bardet et al., 2021), and the impact of moist convection on zonal dynamics in the Jupiter configuration (Boissinot et al., 2024).

These eddy-driven dynamics also give rise to quasi-periodic "eddy-burst events", wherein small-scale instabilities accumulate to cause abrupt stochastic transitions in the zonal jet structure (Bouchet and Simonnet, 2009; Bouchet et al., 2013). During these events the zonal flow is disrupted on a global scale, rapidly transporting momentum and accelerating the zonal jets. These eddy-burst events are qualitatively similar to the large-scale upheavals observed on Jupiter (Rogers, 1995; Fletcher et al., 2011; Pérez-Hoyos et al., 2012; Sánchez-Lavega et al., 2017; Fletcher et al., 2017a,b), albeit markedly more intense and distributed. A particular event of interest is the one seen in Fig. 1. These events happen sporadically in both hemispheres, but during this event the northern hemisphere remained relatively quiescent, with a growing instability from the jet-vortex interaction on the northern edge of the prominent southern cyclone at ~75°S. The early quiescent stage (Fig. 1a) is marked by slowly-varying zonal jets and a near-constant background vorticity structure on the timescales considered here. The disturbed stage (Fig. 1b) is dominated by intense horizontal shear and disruption of the zonal mean state. The final stage (Fig. 1c) is a period of relaxation back to the quiescent state wherein the stable vortices merge over time and deposit their vorticity back into the mean flow via the zonal jets. We note here that while observational studies of Jupiter and Saturn discussed in this paper are typically from the low and mid latitudes, the vortices analysed in this study are exclusively from the polar region, for reasons discussed in Section 3.3.

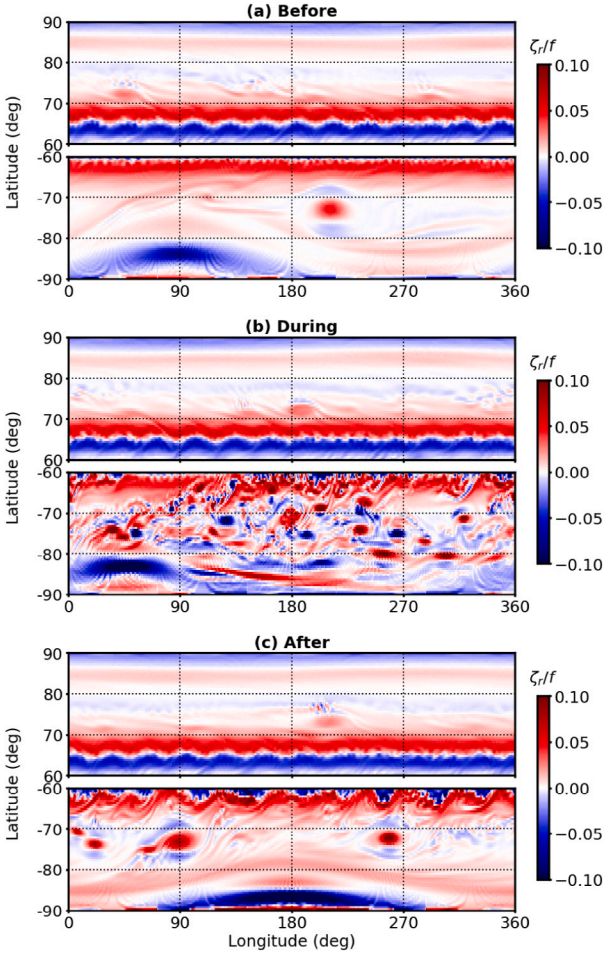

Fig. 1. Relative vorticity field at 700 mbar from the Saturn-DYNAMICO GCM. Time lapse of 1000 model days from the beginning of model year 12 showing the stages before, during, and after a typical eddy-burst event. Vortex merging can be seen with two pairs of clockwise-orbiting cyclones in the southern 0–90° quadrant.

2.2. Vortex detection — general approach

The choice of vortex detection method depends on the nature of the dataset. Sparse datasets of inconsistently-sampled imaging observations and continuously-modelled dynamical fields both present unique challenges. In this work, we treat the seven years of steady-state DYNAMICO model outputs as a "synthetic" observational dataset, which presents the opportunity to explore three distinct methods: visual detection and manual selection in images (previous studies of gas giant vortices, Li et al., 2004; Vasavada et al., 2006; Trammell et al., 2014, 2016), a neural network trained by that approach, and a purely dynamical approach developed for terrestrial oceanic eddies based on modelled dynamical fields (Le Vu et al., 2018). This study explores the advantages and disadvantages of each approach, and quantifies the uncertainties and sensitivities associated with each, with the ultimate goal to study large-scale vortices on Saturn.

This analysis utilises the Saturn-DYNAMICO GCM simulations of Spiga et al. (2020) to probe directly the thermal and dynamical signature of the large-scale vortices (Section 2.1). We assume that the 700-mbar model level corresponds approximately to Saturn's cloud top and provides a meaningful comparison to the cloud-tracked aerosol populations of visible-light observations (Li et al., 2004; Vasavada et al., 2006; Trammell et al., 2014, 2016; Fletcher et al., 2023). Despite small differences in wind fields between levels, there is no particular sensitivity to this assumption since the modelled troposphere in Saturn-DYNAMICO is fairly barotropic and large-scale tropospheric features can persist over many vertical levels. DYNAMICO currently uses a latitudinally-uniform aerosol layer (necessary for radiative balance) and does not resolve cloud microphysics, which renders these results insensitive to aerosol variations.

The three methods produce distributions of vortex location and size (on a latitude–longitude grid). The angular geometry is then converted to geodesic distances on a Saturn-like ellipsoid using the Karney formula for an ellipsoid (Karney, 2012). This is necessary because DYNAMICO assumes a spherical geometry but Saturn is ellipsoidal. The oblateness of Saturn means that spherical geodesic distances can diverge up to 20% zonally and 15% meridionally from the Saturn ellipsoidal case. At each vortex centre we extract temperature, T, zonal wind, U, and meridional wind, V, which are direct outputs of the model and used to calculate higher-order dynamical fields.

In the context of planetary atmospheres and oceanography, the Okubo–Weiss parameter, W, defined in Eq. (1), is a critical tool for distinguishing between rotational and strain-dominated regions within a fluid flow (Okubo, 1970; Weiss, 1991). It has been used extensively to study coherent mesoscale eddies in the terrestrial ocean (Isern-Fontanet et al., 2003; Morrow et al., 2004; Chelton et al., 2007; Chaigneau et al., 2008), and is useful when discussing eddy growth, cyclogenesis and vortex development (merging and splitting) in giant planet atmospheres. By applying the Okubo–Weiss parameter to the DYNAMICO model outputs, we can gain deeper insights into the dynamical behaviour of large-scale cyclones and anticyclones in the Saturn-DYNAMICO GCM, and derive useful diagnostic tools for analysis of vortices in planetary atmospheres.

$$W = \sigma_n^2 + \sigma_s^2 - \zeta_r^2, \tag{1}$$

where $\sigma_n = u_x - v_y$, $\sigma_s = v_x + u_y$, and $\zeta_r = v_x - u_y$ are the *shearing deformation rate*, the *straining deformation rate*, and the vertical component of *relative vorticity*, respectively, where x represents the longitudinal distance and y represents the latitudinal distance. Using this parameter, we explore how the diagnostic metrics developed for the study of submesoscale eddies in the terrestrial ocean (Scherbina et al., 2013; Balwada et al., 2021) can be applied to the interior of GCM the vortices to understand the dynamics close to the vortex core. For comparison to these oceanographic studies we calculate the *horizontal divergence*, δ, where:

$$\delta = u_x + v_y, \tag{2}$$

and combine the two deformation terms into the *lateral strain rate*, α, where:

$$\alpha = \sqrt{\sigma_n^2 + \sigma_s^2} \tag{3}$$

The W parameter is used in the dynamical approach detection step (Le Vu et al., 2018) and later its components are used to characterise the distribution of vortex dynamics (Section 3).

A direct assumption of the manual method (and an indirect one for the neural network) is that a vorticity feature is deemed to be a "vortex" if it has a circular or oval shape with a distinct vorticity magnitude and can be the same or opposite sign to the surrounding flow. This excludes short-lived eddies that are often the progenitors of longer-lived, stable vortices (see Section 2.1), as well as other eddy-dominated circulations like folded filamentary regions (FFRs, Rogers, 1995; Rogers et al., 2006; Wong et al., 2020; Fletcher et al., 2022), and convective/rifted regions.

Vasavada et al. (2006) suggest that the vorticity of each vortex is correlated to the vorticity of the surrounding zonal winds. They admit that they did not measure tangential velocities, and only approximately determined the vorticity sign based on observed behaviour (e.g. orbiting and stability in surrounding shear zone), so it is conceivable that they did not correctly estimate all vorticities in that study. This limitation persists in the assumption of Trammell et al. (2014) that vortices in cyclonic shear regions are themselves cyclonic and vice-versa, though they also admit that this is not necessarily the case (as discussed in Section 3). This is a useful assumption due to the challenges associated with visible-light imaging of aerosol populations but it is not required in the present work using modelled dynamical fields. It is true that these fields used in this work are insensitive to the differences in vortex appearance caused by variations in cloud-top aerosols, so we cannot classify vortices in the same way as Vasavada et al. (2006) and Trammell et al. (2014, 2016). However, they do provide the opportunity to probe the dynamical field directly to find opposite-sign vortices, something that is not possible under the assumption of same-sign selection.

Observed vortices generally exhibit a fairly distinct bright or dark aerosol population embedded in a comparatively uniform bright background. Modelled vortices behave similarly and should naturally overlap with this kind of observation being a roughly distinct vorticity feature in a comparatively uniform background shear. We assume that the edge of an observed and modelled vortex is the boundary within which all of the vorticity of the vortex is contained. Therefore, although not strictly the same, a modelled vortex does provide a good comparison to the observations in this analysis.

However, at smaller spatial scales it becomes difficult to distinguish between small, circular vortices and more ambiguous vorticity features that may be small-scale eddies or transient vortices. We observe the same lower bound of vortex size as the observational studies (discussed in Section 3), but our spatial resolutions differ; 100–150 km/pixel (Cassini/ISS) and 10–526 km/grid point (Saturn-DYNAMICO GCM from pole to equator at half-degree resolution), respectively. This means that we effectively have reduced spatial resolution at low-latitudes, and could be missing the smallest vortices that might be comparable to those in the data. The conclusion is that all model vortices would be visible in the observations, but not all observed vortices are necessarily detectable in the model under these assumptions, so caution is needed when making direct comparisons.

2.3. Manual detection — visual mapping

The "synthetic data" used for the manual detection method use the relative vorticity field, ζ_r. This is comparable to the high-pass filtered images of Vasavada et al. (2006) and Trammell et al. (2014, 2016) since applying a high-pass filter often explicitly involves a similar subtraction of two-dimensional gradients. We tested similar maps of potential vorticity calculated on isentropes (lines of constant potential temperature) where maxima in vorticity are generally more distinct, but they offer no notable improvement on vortex detection at the cost of increased computation.

Of the methods explored in this work, the manual vortex detection is the most direct comparator to observational studies. The model outputs are sampled at each solstice and equinox for seven modelled Saturn years. Later this count will be computed as a seasonal average for comparison to the other two methodologies (which have higher temporal sampling). Seasonal average here is defined as the simple mean of the vortex count in all model time steps in a bin of length one season (90 degrees of solar longitude) and centred on the solstice/equinox of a given season. This temporal sampling and similar fundamental measurement assumptions are intended to represent a "best-case" simulation of what could be expected from long-term giant planet observations. Maps are analysed using the free and open-source Quantum Geographic Information System (QGIS, QGIS Development Team, 2022) to measure features on the vorticity maps by visually identifying the vortex centre and overlaying a "ghost" ellipse until the vortex edge is considered to be completely enclosed. Since the vorticity map is inspected visually, there is notable sensitivity of the output to the contrast of values perceived by the human eye.

To constrain this sensitivity, ten prominent vortices were measured each at five magnifications and four map contrast modes, to estimate the uncertainty in vortex edge detection given that changing gradients can change the shape and size of the boundary. Fig. 2 shows the measured uncertainties as well as the relative contribution of each map mode to the uncertainty. Using average values of the interquartile range (IQR), uncertainty in vortex latitude and longitude is approximately 0.1 and 0.2%, respectively. The zonal and meridional diameters (D_x and D_y, respectively) are each on average ~10%. The uncertainty in zonal and meridional diameters reaches a maximum of 60% in extreme cases where the vorticity gradient across the rim is small (i.e. weak vortex or strong background flow) or where there is significant spatial distortion from the cylindrical map projection (at the highest polar latitudes). It was found that the magnification of the map contributes more uncertainty (up to 50% more) than the contrast of the map.

2.4. Machine learning — artificial neural network

We utilise an Artificial Neural Network (ANN) to search for vortex-like features in the DYNAMICO model outputs, and use the results of the manual study as the training set for this algorithm. This approach is intended to implement the manual method in a more scalable and efficient way.

2.4.1. Network training

To prepare the manually-detected vortices for input into the neural network, the DYNAMICO model fields are sub-sampled according to the spatial bounds of those vortices and down-sampled onto a 6 × 6-point latitude–longitude grid (the specific grid size is arbitrary). Down-sampling like this fixes the number of input features for each vortex and although it removes small-scale atmospheric phenomena from the sample, finer grids do not improve the accuracy of the ANN output at the cost of increased computation time for training and detection.

Each "vortex" in the training set is a grid of T, U, V, ζ_r, and latitude, $|\phi|$, which are reshaped into a one-dimensional array to form

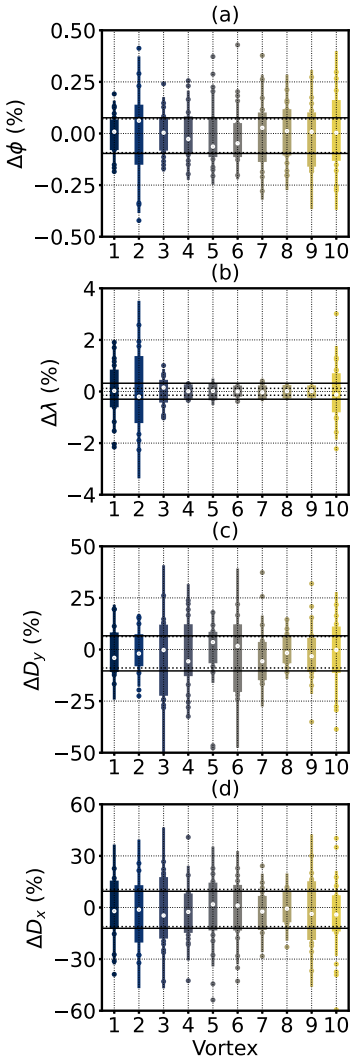

Fig. 2. Measurement uncertainty for the manual vortex detection method showing central latitude and longitude (first and second rows, respectively) and meridional and zonal diameter (third and fourth rows, respectively) for each of 10 prominent model vortices obtained across 20 map configurations. Direct measurements are expressed as a percentage about the mean value for each vortex (coloured points), with the median value (white points), IQR (thick line), and upper and lower quartiles extended by the IQR (thin line). The degree to which the white points vary about zero represents the asymmetry of each distribution. Horizontal lines show the mean (thick) and median (dashed) quartile values. (For interpretation of the references to colour in this figure legend, the reader is referred to the web version of this article.)

the 180 nodes ("features") of the input layer of the network (36 grid points × 5 atmospheric parameters). The windows are also randomly "jittered" up to 20% about each vortex to create examples of off-centre detections that should allow the final algorithm to detect vortices even in cases of sub-optimal alignment. It also ensures that the number of examples of each vortex type is equal, such that each output class has equal weight during training (as an alternative method to asymmetric weighting coefficients, James et al., 2020).

Each network is trained with the range of architectures explored in Section 2.4.2, which produces a maximal training accuracy of 93%. Doubling the sampling density of the grid (thus squaring the number of features) improves this accuracy by 1%, implying that the accuracy is not overly sensitive to the level of detail provided by each sample. This accuracy is more likely to be a reflection of the small sample size of the training set (141 vortices). Such a high accuracy for such a small, and low-resolution dataset implies that the data is not being over-fitted and is promising for future implementations of this neural network detection method (see Section 4).

Feature analysis techniques are used to determine the degree to which each feature (each pixel of atmospheric information) correlates with changes in each of the three output classes "not vortex", "positive vortex", and "negative vortex" (referring to the sign of relative vorticity, ζ). This is useful when there is no clear *a priori* knowledge of what variables to use. On such technique is the Analysis of Variance (ANOVA, James et al., 2020), and when implemented with only these five atmospheric parameters reveals temperature to have the greatest correlation with the output classification. Training the network using only the temperature field actually obtains a test accuracy of 83%, which is remarkable with so few vortices and such low spatial resolution. Broadly speaking, this could mean that the horizontal wind field is not necessary for neural network vortex detection. It may be possible to get a significant fraction of the efficacy of this method with temperature alone, which has implications for imaging data and spatially-resolved thermal retrievals (discussed in Section 4).

2.4.2. Network architecture

In order to avoid over-fitting the data while retaining a good quality classification, the network architecture of ANN approach is optimised as follows. The training data is used to obtain the matrix of weights and biases for a given architecture using the detection algorithm. In order to avoid under-fitting or over-fitting the data, we explore a space of possible architectures to obtain the optimal configuration. The architecture has one input layer with 180 nodes (the reshaped model fields), the intermediate hidden layers, and one output layer with 3 nodes (the three output classes) initialised with randomised weights and biases between the nodes. Each network architecture of 1, 2, and 3 hidden layers with a range of nodes per hidden layer (logarithmically spaced between 2 and 512) is trained fifty times to account for the statistical differences in each randomised matrix of weights and biases, and the *validation accuracy*, A, and *validation cost*, J, are calculated for each architecture. Validation accuracy is simply the ratio of correct predictions and total predictions (equal to one with all correct predictions), and J is a measure of the difference between the real and predicted value (equal to zero with a perfect prediction). It is evaluated using 5-fold cross-validation (because of the statistically small size of the training set), which describes how skilled the network is at operating on an unseen subset of the training data, as a way to evaluate the performance of a given architecture (James et al., 2020). At this stage, J is a more useful metric for constraining the optimal architecture than validation accuracy, since the latter can change with the final implementation of the neural network and detection algorithm.

The global minimum of J represents the optimal configuration of nodes and layers, with node configurations below (fewer nodes) and above (more nodes) the minimum corresponding to under-fitting the data (not well-trained on the training data) and over-fitting the data (only trained on the training data, not generalised for unseen data), respectively. Fig. 3 shows that the optimal configuration in each case is actually the one with the fewest hidden layers (Fig. 3a) and also the fewest overall nodes (i.e. the least complexity). The final chosen network architecture is shown in Fig. 4 and has an input layer (180 nodes), one hidden layer (102 nodes), and the output layer (3 nodes). This architecture was then trained once using all of the training samples, where the labelled test set of samples was used to provide the final measure of ANN accuracy equal to 93%.

2.4.3. Detection algorithm

The final detection algorithm takes the binning scheme from Section 2.4.1, the optimised weights and biases from Section 2.4.2, and applies them to the entire unseen dataset of Saturn-DYNAMICO.

For this, the detection window is passed over each map sequentially in one-degree increments for all latitude–longitude points (ϕ, λ) across a small range of aspect ratios and meridional diameters. From the

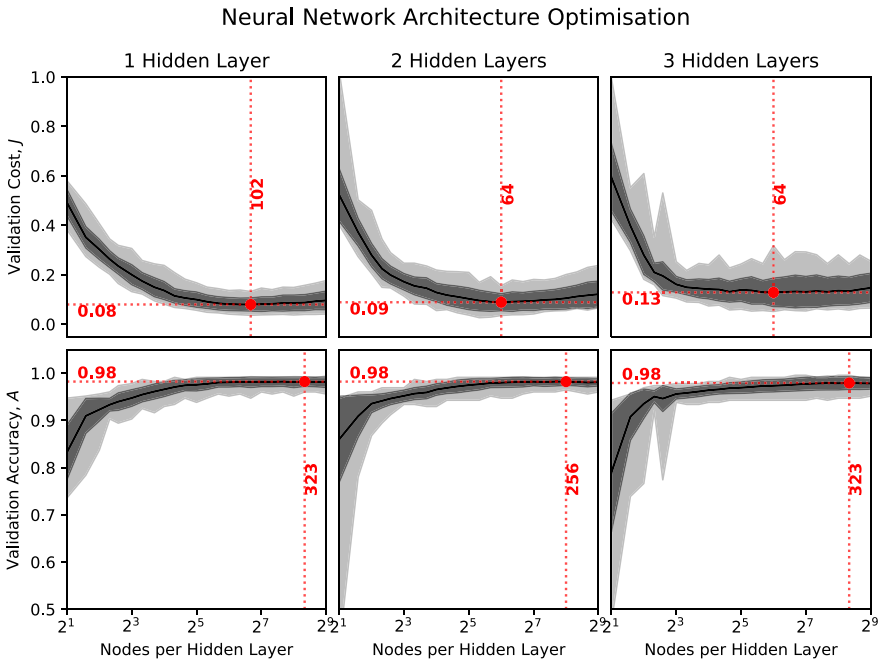

Fig. 3. Validation cost (top) and validation accuracy (bottom) for architectures with 1, 2, and 3 hidden layers, with the optimal configuration highlighted in each. In each panel the solid curve is the mean value, the dark shaded region is one standard deviation about the mean, and the light shaded region is the range.

manual study, it is clear that most vortices exhibit an aspect ratio, $AR = D_x/D_y$, of 1.4, so by fixing the aspect ratio and scanning a small range of meridional diameters ($D_y = 4°$ on the model grid), it is possible to capture the vast majority (>95%) of vortices while substantially reducing the computation time (in fact, size and aspect ratio makes little difference to the ability of the ANN to detect a vortex). For each instance, the contents of a window are evaluated by the network and the region is given a probability according to how likely it is to not contain a vortex or to contain a vortex of either sign. This process generates a two-dimensional probability matrix, $p(\phi, \lambda)$. The peaks in this two-dimensional probability matrix of Class 1 or 2 correspond to cases with a high likelihood of a positive vortex identification. The configurations at these two-dimensional peaks can be found using an assumed probability threshold, and the location and size of those vortices are extracted to form the basis of the analysis of spatial, temporal, and dynamical distributions (detailed in Section 3). The off-centre "partial" detection that jittering offers, effectively increases the range of detection probabilities, widening the probability peaks and reducing the sensitivity of the output to the final selection threshold.

2.5. Dynamical detection - AMEDA

The dynamical approach utilises the Automated Eddy-Detection Algorithm (AMEDA, Le Vu et al., 2018) that was developed for analysis of terrestrial oceanic eddies. Since AMEDA processes directly the dynamical fields (rather than pixel values) the vortex detection is different to the human eye and the ANN, and occurs broadly in three stages. First, it searches locally by passing a fixed window across the global map to find maxima in angular momentum of either sign that coincide with negative maxima in the Okubo–Weiss parameter, W. This corresponds to a location that has high angular momentum and is rotation-dominated, respectively, indicating an eddy or vortex. Then it identifies the largest closed streamline (contour of the streamfunction, ψ) around that point which represents the eddy boundary. Finally, it evaluates the size of the feature with respect to a size-filtering parameter to which vortex detection is highly sensitive and which must be well-justified.

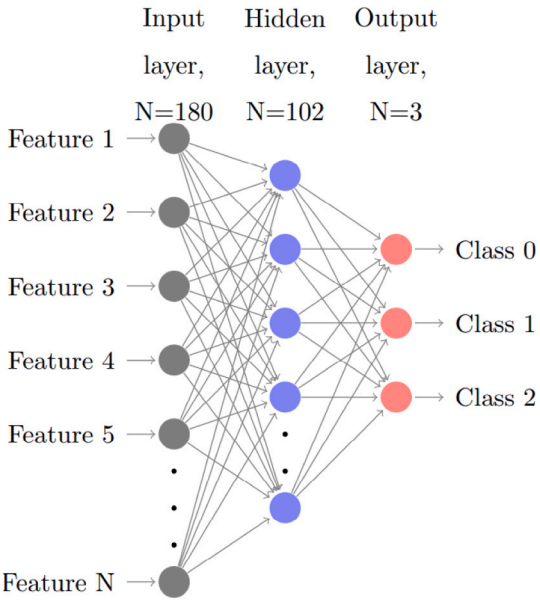

Fig. 4. Schematic of the final neural network architecture. Each input node (grey) represents a feature, i.e. a grid point in the windowed model fields. These are passed to the hidden nodes (blue) then to the output nodes (red) which define the identity of the contents of the window. Bias nodes have been omitted for clarity and arrows represent the neural connections (weights not represented here).

Parametric testing was carried out on all input parameters and the output was found to be slightly sensitive to two scanning parameters but almost entirely sensitive to the size-filtering parameter. The two scanning parameters specified the number of streamlines that are scanned about the angular momentum maximum and the number of points required along a ψ-contour to define a streamline. In both cases we found that a higher or lower detection rate simply implied that it was simply more or less difficult to identify streamlines in the vicinity of the angular momentum maximum, rather than there actually being

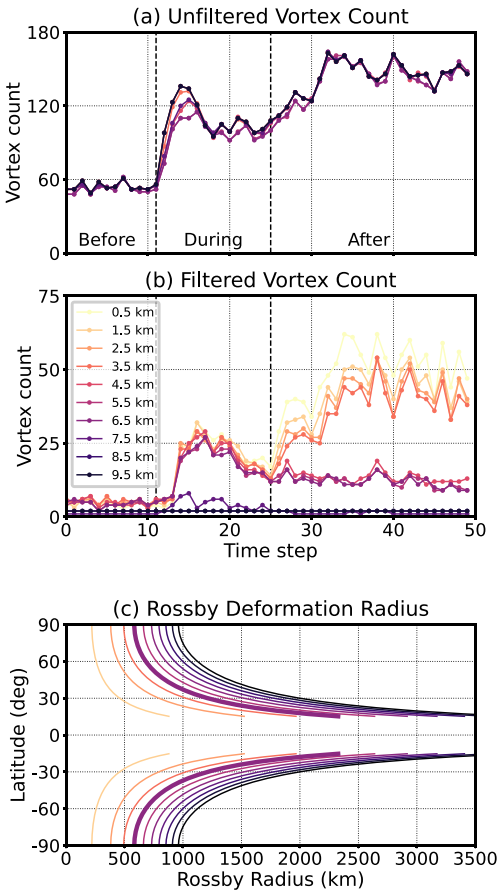

Fig. 5. AMEDA sensitivity analysis of the event in Fig. 1 showing the stages over 1000 model days before, during, and after the eddy-burst. (a) Overall count of detected vortices across range of Rossby layer thicknesses with no spatial filtering, (b) the same count with the spatial filtering applied to the eddy-burst, and (c) the corresponding meridional profiles of Rossby deformation radius. All panels use the same legend. Black dashed vertical lines in (a) and (b) represent the different stages of the event, corresponding to Fig. 1. Thick line in (c) is the 6.5-km solution chosen for this study.

more or fewer vortices found. So it is sufficient to fix these to the values used in Le Vu et al. (2018).

This size-filtering parameter AMEDA uses to isolate large-scale vortices from the small-scale eddies is a tunable spatial scale governed by the Rossby deformation radius, which is the typical scale of large-scale waves arising from baroclinic instabilities and is the characteristic spatial scale at which an eddy may develop into a coherent vortical structure. This scale is not a clear transition, but more a consideration for the approximate scales at which vortices are likely to form. The filtering parameter is defined as the ratio of feature size in pixels to the Rossby deformation radius. This is a reasonable, albeit ambiguous, condition for the rejection or retention of vorticity features. The Rossby scale is particularly difficult to estimate in the atmospheres of gas giants. However, the horizontal resolution of DYNAMICO enables the resolution of eddy-driven instabilities in Saturn's atmosphere, by resolving the Rossby deformation radius on-line, so it is generally not calculated during modelling. Thus, we estimate it through a sensitivity test with AMEDA (reinforcing the observer-oriented focus of this work).

As a null hypothesis, we estimate the *barotropic* Rossby deformation radius, $L_{bt} = \frac{\sqrt{gD}}{f}$ (Holton, 2004), where g is the gravitational acceleration, f is the Coriolis parameter, and D is the thickness of the layer, equal to the distance between the model base and "cloud-top" reference level (~82 km). This gives an upper estimate of $L_{bt} \sim 10\,000$ km in the middle latitudes. This is an order of magnitude larger than the first *baroclinic* Rossby deformation radius, $L_{bc} = \frac{NH}{\pi f}$ (Holton, 2004), inferred from the Brunt–Väisälä frequency, N, of Spiga et al. (2020) at this reference level ($L_{bc} = 1333$ km). Thus, the atmosphere between the model base and the cloud top cannot be represented as a single barotropic layer.

As a lower estimate, the *barotropic* Rossby deformation radius calculated for an atmospheric layer with the thickness of one model level is $L_{bt} = 935$ km, quite similar to the *baroclinic* value inferred from Spiga et al. (2020). Therefore, if we treat this atmospheric layer as being under *baroclinic* conditions for the purpose of obtaining a meridional profile of Rossby deformation radius for testing, we may model it simply using the *barotropic* equation for a suitably shallow layer. By testing a range of these "equivalent layer" thicknesses we obtain a range of Rossby deformation radius profiles and vary the size of the vorticity features that pass through the filter and can assess how sensitive the AMEDA outputs are to our Rossby scale assumptions.

Meridional profiles of Rossby deformation radius associated with barotropic layers of varying thickness are used to determine the magnitude of the filtering parameter as a function of latitude (Fig. 5). If the feature's size is equal to or larger than this scale it passes through the filter. Before applying the spatial filter, AMEDA greatly over-samples the vorticity field, selecting as many distinct maxima of angular momentum as possible, regardless of size. When applying the spatial filtering, the thickest equivalent layers of 7.5–9.5 km (corresponding to the largest Rossby scales) are unable to retain even the largest vortices throughout the event. During the event from time step 11–25, shallower equivalent layers of 0.5–6.5 km (corresponding to smaller Rossby scales) detect all vorticity features whether they are eddies or vortices. After the event beyond time step 25, equivalent layers in the range of 4.5–6.5 km thick (corresponding to Rossby scales of 700–1000 km in the middle latitudes) filter out most of the small-scale eddies and leave most of the large-scale vortices.

This filtering is imperfect as it is possible to lose the smallest of the coherent vortices. However, in the context of the manual and ANN methods (see Section 3) these smallest vortices do not comprise a significant portion of the vortices found in the model. Fig. 5 shows that DYNAMICO does in fact capture the clear selection of spatial scales for cyclogenesis that is expected from first principles.

Following the filtering step, AMEDA returns the location and spatial bounds of each vortex, producing the spatial distributions discussed in Section 3. Additionally, AMEDA automatically calculates the mean radius of each vortex as a circle with the same area as one enclosed by the closed streamline. From this, a mean velocity profile is derived from the circulation along the closed streamline (Le Vu et al., 2018). The peak of the mean velocity profile is reasonably assumed here to be the vortex edge. The assumption of circularity is used here only for this calculation as the actual shape is retained for the purposes of studying the spatial structures. This step is intended as a way to explore the internal dynamics of each vortex and the results are shown in Fig. 10 and discussed in Section 3.

3. Results

The distributions of location, size, shape, zonal winds, and vortex intensity generated by these three methods are compared below, with the total vortex count, annual count rate derived from the seasonal average of counts, and mean aspect ratio summarised in Table 1. Additionally, the AMEDA results are used to explore vortex dynamics along vortex boundaries with the edge velocity profiles and interiors with an inter-comparison of the three Okubo–Weiss parameters. Finally, a short discussion of the planetary Burger number (defined in Section 3.5) is proposed, discussing the great diversity of polar regimes and configurations of polar vortices in the giant planets, and implications for future study.

Table 1
Summary of primary statistics of vortices in the GCM for each method. Columns show the vortex sense as determined by the sign of the planetary-normalised relative vorticity, ζ/f (positive for cyclones and negative for anticyclones), the total raw vortex counts, and the annual count rate calculated from the seasonal average of raw vortex counts over 7 model years. All counts are separated by vortex sense and hemisphere (NH and SH for north and south hemispheres, respectively). Aspect ratios (AR) are expressed as a global average, separated only by vortex sense.

Method	Sense	Total vortex count			Count rate (year^{-1})			Mean
	(ζ/f)	Global	NH	SH	Global	NH	SH	AR
Manual	Both	141	63	78	20.14	9.00	11.14	–
	+ve	82	33	49	11.71	4.71	7.00	1.44
	−ve	59	30	29	8.43	4.29	4.14	1.13
ANN	Both	96 404	51 844	44 560	48.59	26.61	21.97	–
	+ve	58 729	27 811	30 918	28.81	14.48	14.34	1.54
	−ve	37 675	24 033	13 642	19.77	12.13	7.64	1.38
AMEDA	Both	552	273	279	17.73	9.54	8.19	–
	+ve	321	131	190	10.19	4.93	5.26	1.47
	−ve	231	142	89	7.54	4.61	2.93	0.98

3.1. Spatial and temporal distribution

All large-scale vortices in the Saturn-DYNAMICO model are clustered in latitude and are present in regions of cyclonic and anticyclonic shear in the zonal wind (as in Vasavada et al., 2006). They are found exclusively beyond 60° latitude in each hemisphere at the highest-latitude westward jets, with slightly more in the south (as in Trammell et al., 2014). This strong correlation with the jet locations follows the poleward migration of the jet structure that was reported in Spiga et al. (2020), further confirmation that these vortices are reproducing expected behaviours. Unlike the observed vortices of Trammell et al. (2014, 2016), the model produces no large-scale vortices at latitudes lower than this. This is likely because the criterion for barotropic instability, a necessary but insufficient condition for generation of these vortices (Spiga et al., 2020), does not change sign in the domain of the low and mid latitudes. Even if they were produced, the spatial resolution of the model (one half-degree grid cell at the equator spans ~500 km), they would be difficult to detect with these methods since the median size vortex would be 2–4 grid points (1000–2000 km across), as discussed in Section 3.4. In contrast, low- and mid-latitude vortices towards the larger end of the size distribution (>10 grid points) would be easier to detect.

The manual method has lower temporal sampling than the automated methods so we express the vortex counts as a seasonal average as also a way to partly control for repeated sampling of long-lived vortices that span multiple model time steps in a given season. This is a moderate sampling bias as we do not sample unique vortices, but it is sufficient to build up a statistical view of the instantaneous structure of vortices. The manual method is treated as a seasonal average by experimental design (see Section 2.3), so the ANN and AMEDA methods are averaged onto the same temporal grid by averaging the vortex counts over multiple model time steps per season. The raw vortex counts and annual count rates (derived from the seasonal averages) are found in Table 1. The automated methods have a common temporal sampling, so difference in counts between the two methods directly reflects differences between the neural network and dynamical approaches.

Comparing the seasonally-averaged vortex counts, the manual method found 141 vortices in total, while the ANN and AMEDA methods found 340 and 120, respectively. Fig. 6 shows the vortex counts and locations as a function of time for each of the three methods. While the methods return similar seasonally-averaged vortex count over time, there are some differences that reflect the fundamental differences between them. This is seen clearly in model year 14, in which there was a particularly large eddy-burst event that left the south polar region very disrupted with a disorganised structure of eddies that progressively merged into fewer and larger vortices. During the disrupted state, the human eye can reasonably distinguish near-circular vortices from the smaller-scale eddies. However, AMEDA relies on the clear detection of closed streamlines and has difficulty in resolving anything other than the most dominant polar cyclone and anticyclone for most of the outburst. Another notable difference is the 3–10 times higher detection rate of the ANN method in model year 8.

With the benefit of the long time series of simulated model years, there is a tentative seasonal variability in vortex count but not in spatial distribution (the latter is in agreement with observations by Trammell et al., 2014, 2016). We also see a lack of variability associated with the long-term changes in atmospheric temperature, supporting the conclusion of Trammell et al. (2016) that large-scale thermal structure and circulation are not directly affected by the temporal variation of vortices. However, there is an inter-annual shift from more northern vortices earlier in the model to more southern vortices later, but this is likely incidental, being a function more of the spontaneous eddy-burst events than any long-term changes in atmospheric structure.

3.2. Size and shape distribution

The vortices generated in Saturn-DYNAMICO are generally much larger than observed vortices. This is more likely due to a greater latitudinal spacing between the modelled zonal jets than the characteristic jets of the planet Saturn. This renders absolute estimates of vortex size useful when comparing model parameterisations (and thus modelled jet structures), but not particularly useful in direct comparison to observations. However, the overall shape of the size distribution can provide relative insights to those of the planet Saturn.

With all methods we see an order-of-magnitude correlation between overall size and Rossby deformation radius, which is expected by Trammell et al. (2016) and reinforced by the efficient eddy filtering in AMEDA. Fig. 7 shows the distribution of mean vortex radius, $\bar{R} = \frac{1}{2}(D_x + D_y)$, in units of Rossby deformation radius. With the manual and AMEDA methods we do not find any vortices below ~1000 km (or 1 L_{bt}, the systematic assumption made to reject eddies below this characteristic spatial scale). However, the manual method do not have this assumption, yet reproduce the same minimum vortex size as AMEDA and observations (Trammell et al., 2014, 2016), confirming the utility of the filtering assumptions for AMEDA. Note that ANN-detected vortices are often smaller than this threshold, suggesting an erroneous detection of features smaller than the Rossby length scale.

Fig. 8 shows that in most cases the vortices peak towards smaller values at ~ 5000–7000 km, and have a long tail extending to ~15 000–18 000 km in very low concentrations (≤1% of vortices). In the AMEDA case there is a sharp drop-off after 7000 km in both the zonal and meridional directions. Since eddy filtering is performed with respect to Rossby deformation radius, it is not clear there should be such a strong selection of absolute spatial scale in comparison to other methods. Vasavada et al. (2006) observe a wide range of sizes in regions of cyclonic shear, but despite a few exceptionally-large cyclones, wide distributions are seen in all regions independent of shear sense. The maximum size of modelled vortices is greater than observations by a factor of two (Voyager/ISS, Rogers, 1995) and three (Cassini/ISS, Trammell et al., 2014, 2016). So while the model spatial resolution at lower latitudes might preclude detection of the smallest vortices, vortices of this larger size were simply not observed in the atmosphere of Saturn, with the exclusive exception of the polar vortex as measured by the Pic du Midi (7000–11 000 km, Sánchez-Lavega et al., 1993, 1997).

Fig. 8 shows the distributions of zonal and meridional diameters, organised by aspect ratio and shape. Most vortices are circular or zonally-oblate across all methods (not surprising in the manual and ANN case since it is an explicit assumption), implying a greater propensity for vortex growth in the zonal direction than the meridional direction. The manual approach appears to show no clear differences

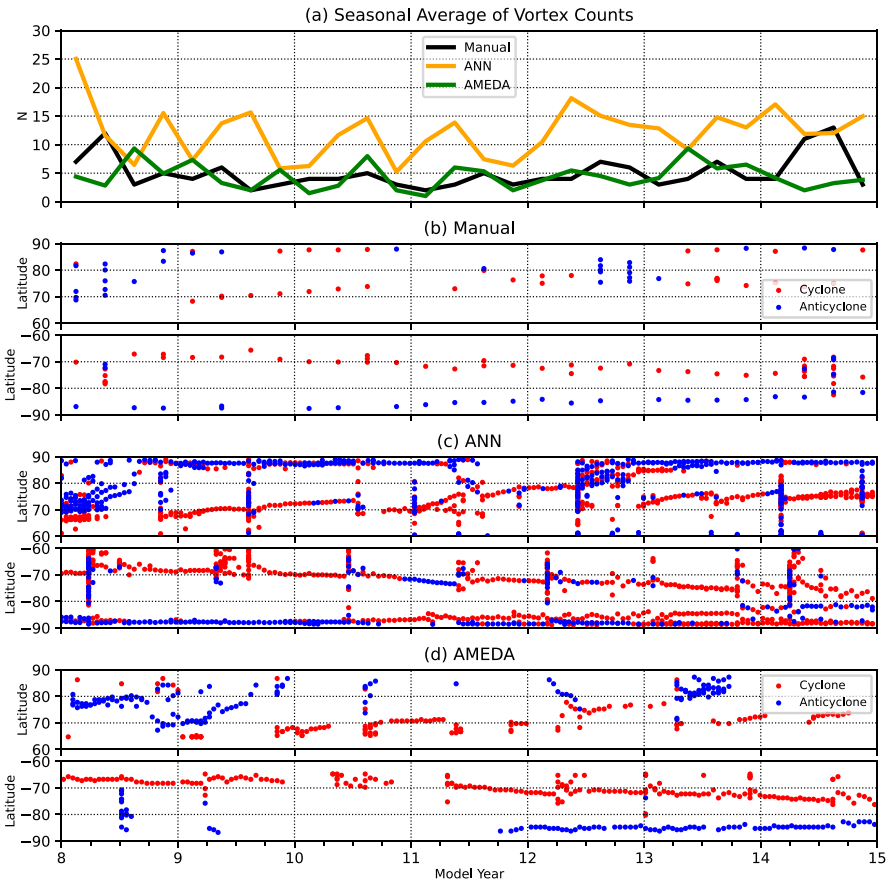

Fig. 6. Time series of (a) seasonally-averaged vortex counts and (b–d) spatial distribution of vortices separated by vortex sense for the manual, ANN, and AMEDA methods, respectively.

in shape between cyclones and anticyclones with a least-squares fit through the entire distribution (in agreement with Trammell et al., 2016, but with more circular vortices overall). The expectation from observations should be more like the AMEDA result with anticyclones being more circular and with a narrower range of aspect ratios, and cyclones having a much wider range of aspect ratios and sometimes being very zonally oblate (e.g. anticyclonic white ovals compared to cyclonic brown barges, Rogers, 1995; Morales-Juberìas et al., 2002; Legarreta and Sánchez-Lavega, 2005; Rogers, 2007; Rogers et al., 2010; Orton et al., 2015; Fletcher et al., 2017a). Indeed this is exactly the case for the most common value of aspect ratio for all methods, seen in Table 1.

3.3. Vortex winds

Barotropic instability seems to be a necessary but not sufficient condition for cyclogenesis in DYNAMICO. This is because cyclogenesis occurs exclusively at the highest-latitude westward jets, where the Rayleigh–Kuo criterion for barotropic instability is frequently violated, and not seen at the barotropically-stable low and middle latitudes where it is not violated (Spiga et al., 2020).

If we treat each vortex centre as instantaneously stationary with respect to the mean flow, we can get an estimate of the zonal wind at the vortex location which we can use as a proxy for drift rate. Fig. 9 shows that most vortices form very close to the average zonal-mean zonal-wind profile for the entire DYNAMICO simulation with a small fraction being associated with high rates of prograde and retrograde drift about the mean flow. Cyclones and anticyclones generally exhibit similar ranges of drift velocities throughout the model, but the largest drift rates are exhibited by the anticyclones. Future investigations will use the extended functionality of AMEDA to track the short-term evolution of vortices as described in Le Vu et al. (2018), including direct measurements of the drift rate and vortex interactions (merging/splitting events).

Vortex generation and stability can be understood through the mechanism of cyclogeostrophic adjustment during frontogenesis according to Shakespeare (2016). In the idealised case, a straight, uniform pressure gradient field can establish a straight front, a boundary that separates air masses with differing characteristics (e.g. density, temperature, pressure, or wind speed). The front is increasingly subject to Coriolis acceleration as it increases in latitude, causing frontal curvature through geostrophic adjustment. This curvature generates a centripetal acceleration which acts to further increase curvature in proportion to the ratio of centripetal and Coriolis acceleration, i.e., through *cyclogeostrophic* adjustment. Frontal velocities become so high along this increasingly curved front that eddy growth is strongly limited and a distinct vortex may be established.

Stable fronts like those of the steady-state thermal field in the Saturn-DYNAMICO GCM can suddenly be subject to rapid forcing from the kind of quasi-periodic large-scale eddy-burst events that are ubiquitous in the model (Spiga et al., 2020). This could reasonably result in the latitudinal deviation required to cause geostrophic adjustment. Then surrounding conditions, those which vary on the scale of several model grid points (a few degrees in latitude or a few thousand kilometres, comparable to the upper range of the terrestrial mesoscale, 200–1000 km) need only be sufficient to encourage further curvature through centripetal acceleration and subsequent vortex stabilisation. So it should be the surrounding conditions which determine the eventual structure and dynamics of the GCM vortices.

Fig. 10a shows that all vortices found in the model are cyclostrophic yet it is not clear how important geostrophic curvature is to the vortex dynamics in DYNAMICO. According to Shakespeare (2016), if at least

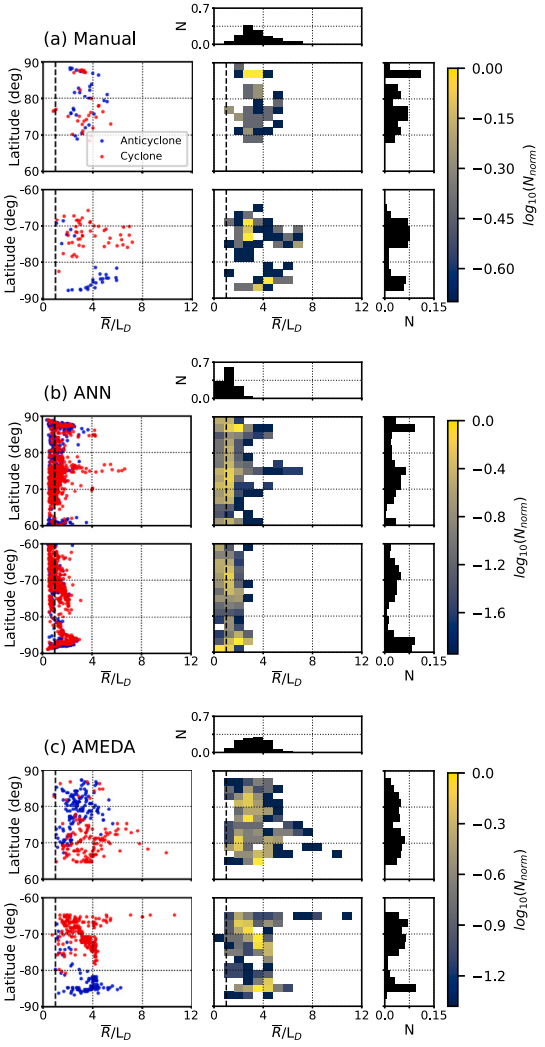

Fig. 7. Size distribution of vortices in the GCM for (a) manual, (b) ANN, and (c) AMEDA methods. (Left) Rossby-normalised average size as a function of latitude as a scatter separated by vortex sense, and (right) 2D joint probability density histogram of number density, N, with 1D histogram components bounding the relevant axis. 2D histogram data is normalised to the data range, such that $N_{\text{norm}} = \frac{N-N_{\text{min}}}{N_{\text{max}}-N_{\text{min}}}$, and colour values are distributed logarithmically as $\log_{10}(N_{\text{norm}})$. Dashed line corresponds to $\bar{R}/L_D = 1$. (For interpretation of the references to colour in this figure legend, the reader is referred to the web version of this article.)

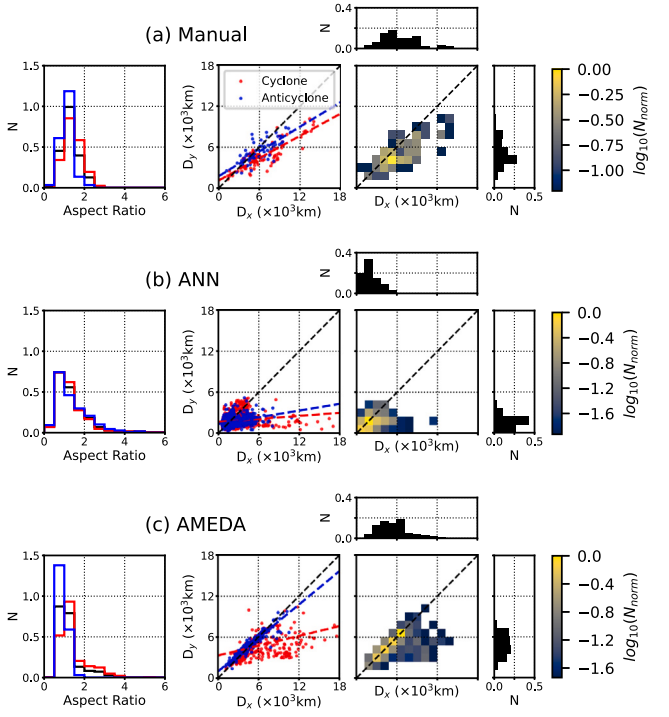

Fig. 8. Shape distribution of vortices in the GCM for (a) manual, (b) ANN, and (c) AMEDA methods. (Left) 1D histogram of aspect ratio and (centre) scatter of zonal and meridional diameters separated by vortex sense, and (right) 2D joint probability density histogram of number density (colour scale based on that of Fig. 7).

one of the following conditions is true, the curved fronts (eddies or vortices) can be considered to be in *cyclogeostrophic* balance: (i) frontal velocity (analogous to vortex edge velocity, V_{max}) is high, (ii) radius of curvature (radius at maximum velocity, R_{max}) is small, or (iii) latitude, ϕ (or Coriolis parameter, f), is small. From Fig. 10b it can be reasonably concluded that the former two conditions are satisfied, even though the latter is clearly not, since all vortices are found beyond 60° of latitude (indeed, on a quickly-rotating body like Saturn, it is difficult to have a small Coriolis parameter unless very close to the equator). Therefore, we may represent the cyclogeostrophic curvature as the ratio of the centripetal and Coriolis accelerations, the so-called *cyclogeostrophic* Rossby number, $C = v/fr$, Mkhinini et al. (2014) and Shakespeare (2016). Cyclogeostrophic curvature is important to the dynamics if C is non-negligible.

Fig. 10(c–f) shows that the cyclogeostrophic Rossby number, C, is indeed non-negligible (<0.18) for the vortices, thus cyclogeostrophic curvature is modifying the speeds by up to 18% with respect to the geostrophic prediction. This is below the range found for jovian vortices measured by Voyager/ISS and the Galileo instrument (Legarreta and Sánchez-Lavega, 2005). However, it is similar to low- and mid-latitude terrestrial oceanic eddies, which have observed C values of 0.1–0.3 for the Gulf Stream meanders (Liu and Rossby, 1993), and 0.25 in the equatorial Pacific (Flament et al., 1996; Holmes et al., 2014) and the Kuroshio Extension in the northwestern Pacific (Niiler et al., 2003). Here we also see that C is moderately positively correlated with V_{max} ($r = 0.854$) and minimally with ϕ and f ($r = 0.441$ and 0.410, respectively), and negligibly negatively correlated with R_{max} ($r = -0.263$). Conversely, C values close to zero indicate that curvature is not important and the front is close to geostrophy, which is roughly true for the slowest, lowest-latitude, and largest vortices observed here.

3.4. Vortex dynamics

Theory predicts that frontal curvature about a warm-core vortex (terrestrial anticyclone) should act to increase velocities, and curvature about a cold-core vortex (terrestrial cyclone) should decrease velocities (Shakespeare, 2016). This is reversed for vortices in the upper troposphere of gas giants due to the lack of a lower boundary layer (e.g. like the terrestrial surface) inverting the energy dissipation scheme (Ingersoll et al., 2021). Furthermore, higher frontal velocities in opposite-sign vortices (vortex sense has opposite sign to background shear) should act to make them less stable and more prone to dissipation or instability during adjustment (Hoskins and Bretherton, 1972; Rudnick, 2001; Scherbina et al., 2013), reducing the number of opposite-sign vortices produced in the model.

Fig. 11 shows the distribution of planetary-normalised relative vorticity, ζ_r/f, the ratio of the relative and planetary terms and a measure which is always positive for cyclones and negative for anticyclones.

Since we do not observe warm-core cyclones with high frontal velocities, it might be that they are forming in the Saturn-DYNAMICO model but dissipating more quickly than their anticyclonic counterparts. If cyclones are generally more likely than anticyclones to be dissipated when they are of opposite sign to the shear region, then

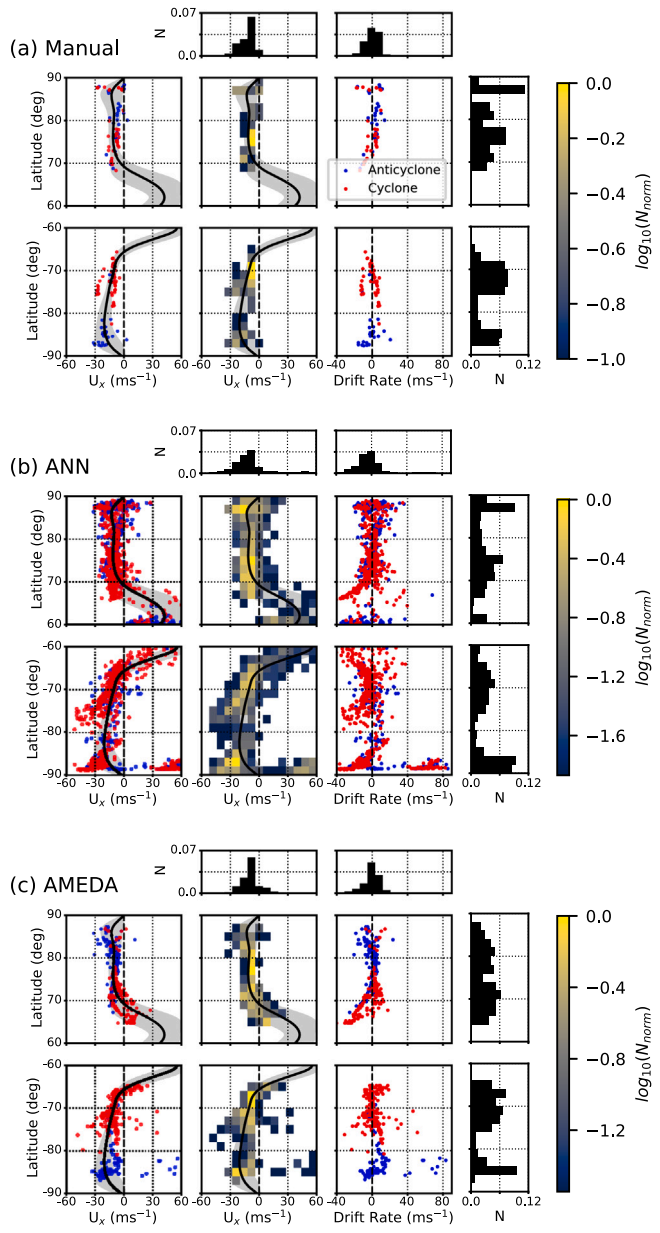

Fig. 9. Local zonal wind and drift rates of vortices in the GCM for (a) manual, (b) ANN, and (c) AMEDA methods. (Left) scatter of the zonal wind velocity at vortex centre, (centre) 2D joint probability density histogram of number density (colour scale based on that of Fig. 7), and (right) scatter of the relative velocity of the vortices with respect to the mean flow. Scatters are separated by vortex sense.

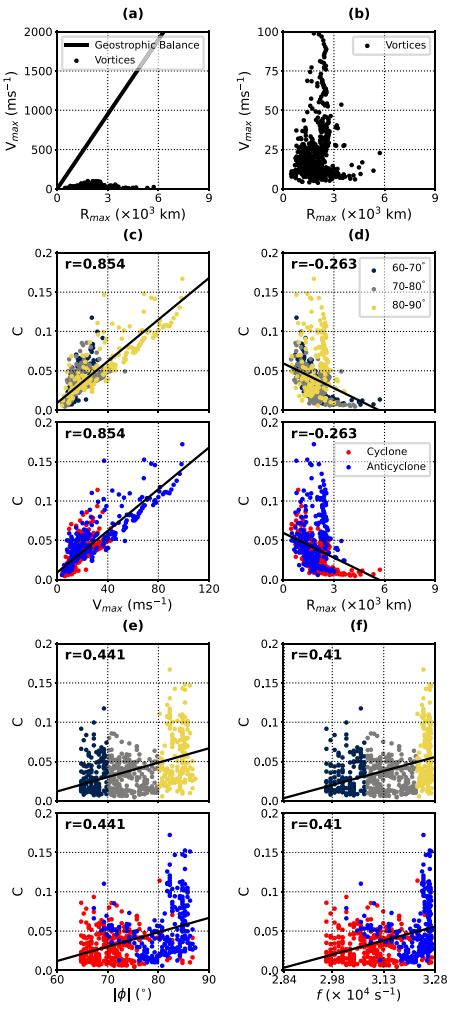

Fig. 10. Vortex dynamics in the polar regions as measured by AMEDA. Vortex edge velocity as a function of vortex radius for all detected vortices (black points), (a) with and (b) without the geostrophic balance condition assuming $Ro = 1$ (black line). Cyclogeostrophic Rossby number, C, as a function of (c) V_{max}, (d) R_{max}, (e) $|\phi|$, and (f) f, separated by latitude domain, and with linear fit and Pearson correlation coefficient.

cyclones should be generally less common in anticyclonic shear regions than anticyclones are in cyclonic shear regions. Indeed, unlike the observations of Vasavada et al. (2006) but similar the theoretical predictions of Scherbina et al. (2013) (allowing for the inversion of the momentum dissipation scheme above), the modelled vortices are actually more common in cyclonic shear regions, despite the dominant selection mechanism of anticyclones. This asymmetry is reflected in Fig. 11 and is more pronounced in the north. The origin of this hemispheric asymmetry is not clear, but is likely simply a result of the sporadic eddy-bursts.

In the model, the dearth of anticyclones relative to cyclones ($n_a/n_c \approx 0.7$) seen in Table 1 and Figs. 11, 12, and 13 is in stark contrast to the putative nature of the upper troposphere of the gas giants which are expected to have an anticyclonic bias. However, in the Saturn-DYNAMICO model the cyclonic shear regions are simply much larger than anticyclonic shear regions, so even with a symmetric dissipation, same-sign selection implies that we might still expect more cyclones overall. Essentially, if the zonal wind profile looked more like Saturn the vortex distributions likely would as well.

We note here that the planetary-normalised vorticity of the ANN method is an order-of-magnitude lower than the others. The dominance of low vorticities can be explained by the prevalence of sub-Rossby scale features, but it is unclear why we are missing the largest vorticities, especially since all methods produce similar size distributions.

Since the AMEDA method reliably detects a large number of vortices, with associated quantitative diagnostics, we use that dataset to further explore the three Okubo–Weiss parameters. These three parameters provide a useful diagnostic for vortex dynamics that will be used as a metric for future comparative studies (see Section 4). They are calculated for all detected vortices and compared to the planetary state overall (all polar grid cells within ±60–90° latitude). The probability density histograms are displayed in Fig. 12 and combined in Fig. 13 to give a more general view of rotation and deformation characteristics, as a comparative metric to the terrestrial oceanic studies that inspired this aspect of the analysis (Rudnick, 2001; Scherbina et al., 2013).

The vorticity distributions in Fig. 12a and d are that of 11c and show the same northern symmetry of intensity and vortex sense and the

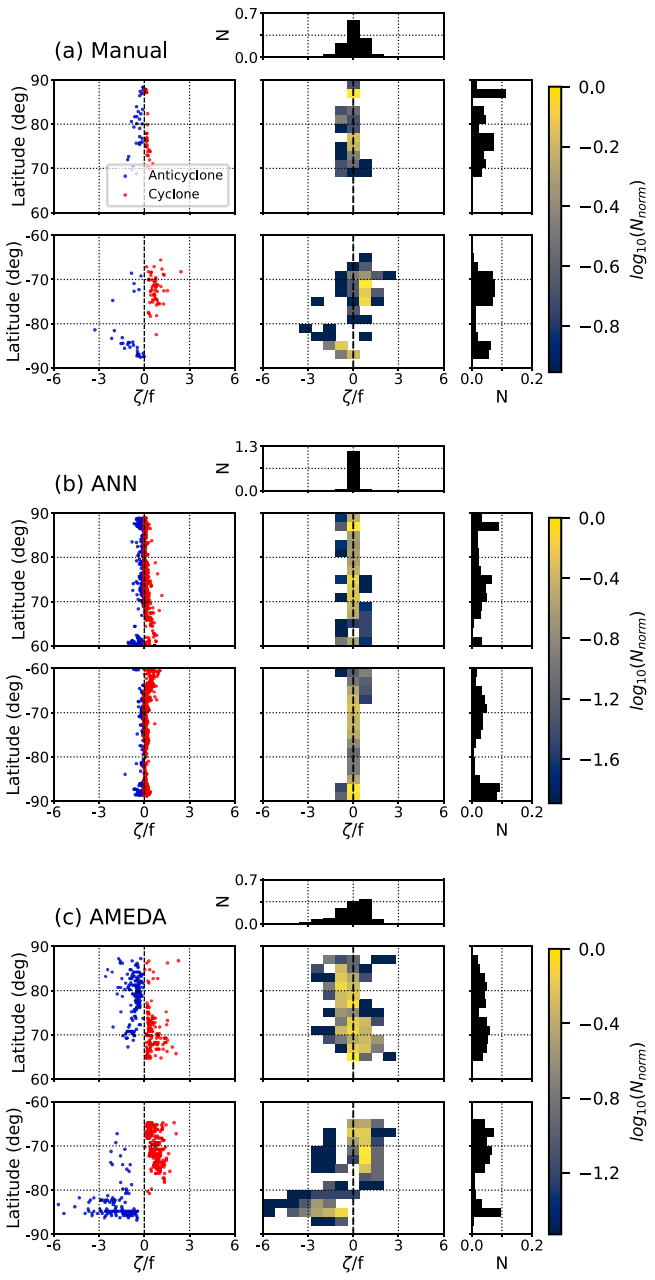

Fig. 11. Distribution of vortex intensities in the GCM for (a) manual, (b) ANN, and (c) AMEDA methods. (Left) scatter of the planetary-normalised relative vorticity at vortex centre separated by vortex sense, (right) 2D joint probability density histogram of number density (colour scale based on that of Fig. 7).

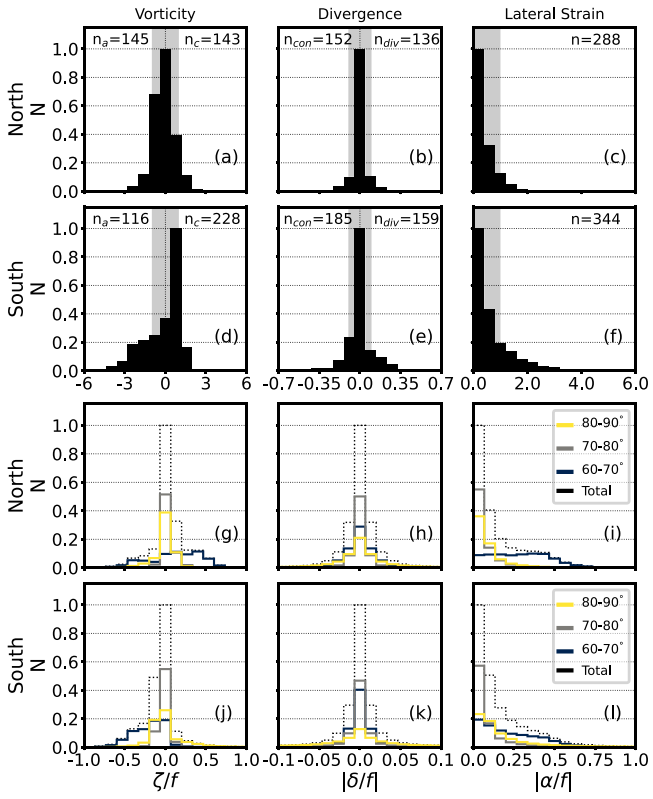

Fig. 12. Distribution of Okubo–Weiss diagnostics. Histograms of planetary-normalised vorticity, divergence, and lateral strain separated by hemisphere and normalised to maximum counts for all vortices (*a–f*) and all model grid cells (*g–i*). Coloured histograms (*g–i*) show the parameters in the same latitude ranges as Fig. 10. (For interpretation of the references to colour in this figure legend, the reader is referred to the web version of this article.)

southern asymmetry with a higher number of cyclones and stronger anticyclones. This means that weak vortices are more likely to be cyclonic, moderately-strong vortices are more likely to be anticyclonic, and the strongest vortices are always anticyclonic. A similar hemispheric trend is seen in the divergence distribution with a slightly more pronounced northern asymmetry and much smaller overall magnitudes compared to vorticity and strain. The distribution of lateral strain rates adds to this picture in the same way, showing that vortices in the south polar region are generally a lot more dynamically diverse than those in the north.

This kind of hemispheric asymmetry is difficult to observe on gas giants without highly-resolved imaging and cloud-tracked wind measurements of both polar regions. However, Siegelman et al. (2022a) characterise the north polar region of Jupiter with Juno/JIRAM images and show that vorticities within the circumpolar vortices can reach magnitudes on the scale of the planetary vorticity ($\zeta/f \sim 1$). They observed much smaller relative magnitudes of horizontal divergence, δ (Eq. (2)), similar to DYNAMICO, implying that these vortices are dominated by two-dimensional turbulence at these spatial scales. Future studies that explore the south polar region in the context of these JIRAM images and this dynamical study will add much-needed context to the study of vortex dynamics.

Joint probability density histograms in Fig. 13 show the relative shapes of these distributions. Considering the lateral strain rate, α (Eq. (3)), with respect to the vorticity gives an indication of whether the vortex is in an eddy regime ($\alpha < |\zeta|$), a shear regime ($\alpha = |\zeta|$), or a strain regime ($\alpha > |\zeta|$). For example, the peaks of the zonal jets are a purely shear regime and are seen in the clustering of values around the diagonal lines in Fig. 13e. Fig. 13c shows that smaller, weaker vortices lie close to but below the shear regime, reflecting their short-lived and transient nature, forming and dissipating quickly following a large eddy-burst event. However, some small vortices are also strongly rotation-dominated despite their weak vorticity, which is more true for anticyclones than cyclones. Anything in between these lines in the eddy-shear regime corresponds to a cyclogeostrophic front with varying magnitudes of rotation.

Finally, we gather together all of the statistical parameters from this work to summarise their relative differences between all cyclones and anticyclones detected in the Saturn-DYNAMICO simulation. All distributions are normalised so that they vary between 0 and 1. This removes absolute differences between the parameters and instead emphasises the relative distributions for cyclones and anticyclones. The multivariate distributions in Fig. 14 reinforce the conclusion that cyclones are

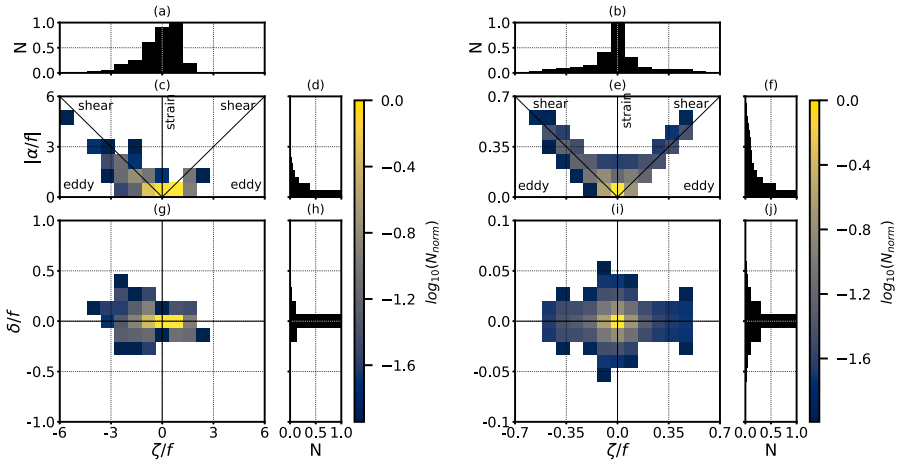

Fig. 13. Distribution of Okubo–Weiss diagnostics. 2D joint probability density histogram of number density (colour scale based on that of Fig. 7) constructed from the global distributions of rotation and deformation terms in Fig. 12. The left group shows values for the vortices (*a, c, d, g, h*) and the right group shows values for all grid cells in the polar regions (*b, e, f, i, j*). The black diagonal lines correspond to one-dimensional shear flow and the horizontal line $|\alpha/f| = 0$ corresponds to solid-body rotation.

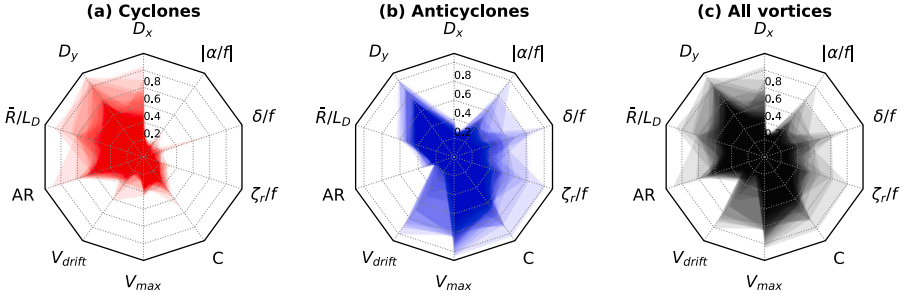

Fig. 14. Multivariate distributions of all statistical parameters for all vortices, separated by vortex sense. Zonal-mean zonal wind is omitted since that is unique to the GCM and is not strictly a vortex characteristic. Each axis contains the absolute-normalised values such that each parameter varies between 0 and 1. Colour opacity reflects the number density of vortices along each axis (more transparent colours means fewer vortices exhibit that value). The sequence of parameters is in no particular order. (For interpretation of the references to colour in this figure legend, the reader is referred to the web version of this article.)

more spatially diverse (they exhibit a greater range of sizes and shapes) and anticyclones are more dynamically diverse (they exhibit a greater range of edge velocities, drift rates, Okubo–Weiss parameters), and they provide a useful "fingerprint" for future comparative studies of vortex statistics.

3.5. Polar regimes

The polar regions of the Saturn-DYNAMICO GCM exhibit a great diversity of circumpolar jet and vortex configurations, at different times resembling all of the giant planets in the Solar System. O'Neill et al. (2015, 2016) comprehensively investigate the importance of moist convection and energy dynamics in driving polar cyclones on gas giants. Brueshaber et al. (2019) further explore the planetary Burger number, $Bu = (L_D/a)^2$ (Read, 2011), as it relates the Rossby deformation radius and corrected polar radius, a, to the structure of polar vortices as observed on Jupiter, Saturn, Uranus, and Neptune. They found that the value of the Burger number strongly determines the configuration of polar vortices, with small values ($1–1.7 \times 10^{-4}$) corresponding to a jovian configuration of multiple, small, and often circumpolar vortices, with a transition region followed by a kronian regime (1.4×10^{-3}) and a general regime of the Ice Giants ($1–7 \times 10^{-2}$), both with a much stronger, pole-centred, and stable cyclone.

Using the Rossby deformation radius inferred in Section 2.5 and the mean planetary radius of Saturn, $a = 58\,232$ km, gives estimates of Burger number of $1.9–2.3 \times 10^{-4}$ beyond ±60°. This is directly comparable to the jovian regime identified by Brueshaber et al. (2019), half that of the transition region, and one eighth that of the kronian regime.

Inspecting the polar regions of the GCM through the many cycles of quiescence and disruption, it is clear that the Saturn-DYNAMICO model actually exhibits all of the polar vortex configurations identified by Brueshaber et al. (2019), despite the slowly-varying zonal flow with time. However, using this formula the theory predicts that the Burger number regimes of Brueshaber et al. (2019) greater than jovian should not occur on Saturn at all, despite the clear variability in Saturn-DYNAMICO vortex configurations. They show that the vortex configuration is strongly determined by the Burger number, but we see here that the configuration may in fact vary weakly with Burger regime in the DYNAMICO GCM. From this work, their values of Burger number seem too high, and those magnitudes do not allow for a commensurate change in vortex configuration. We believe this points to key differences between the global resolution of eddy-to-mean interactions of DYNAMICO, and the idealised polar simulations of Brueshaber et al. (2019). In addition, perhaps the picture is more subtle or complex, such that defining vortex configuration regimes by Burger number incompletely captures the details of the relationship between the two.

4. Conclusions

Large-scale vortices in the Saturn-DYNAMICO GCM occur spontaneously in the model as a result of well-resolved eddy-to-mean interactions. While the spatial, temporal, and dynamical trends are broadly consistent with the historic record of vortices on the giant planets, there are still important differences that are explainable and present the opportunity for future exploration through modelling and comparison to observations.

4.1. Strengths and limitations of the methods

The manual method has necessarily limited temporal sampling compared to the automated methods, but seems to be as reliable as observational studies. However, despite the benefits of improved assumptions, a direct sense of the vorticity field, and multiple modelled Saturn years, the result still does not accord with the some expectations of giant planet vortices (most importantly, the lack of a clear vortex-sense asymmetry in vortex shape). This could come from multiple sources; a statistical effect due to the small sample size, flawed input assumptions, inherent uncertainty in human-visual detection, inherent differences between the model and the planets, or other unknown sources (making statistical conclusions difficult). Regardless, since there is a similar lack of vortex-sense asymmetry in previous observational studies, we conclude that we must share the same limitations and biases as those studies. This method is best used with sparse planetary imaging datasets or short model timescales, but is considered less robust than the dynamical method in the latter case.

Since the neural network is trained with the results of the manual method, it is necessarily constrained by the same assumptions, and despite its highly non-linear pattern recognition it can only search for things that look like manually-detected vortices. The benefit to this approach is that the algorithm can be applied to the entire time series of model outputs and can incorporate in its detection the thermal and dynamical fields simultaneously. During network optimisation, we found that the optimal configuration is the one with the least complexity, implying that the problem could be simpler than initially expected. From the feature analysis, we found that temperature correlates the most to the positive classification of a "vortex", so it may still be possible to perform this kind of analysis only with that variable. This has positive implications for future work which will include a deeper exploration of the network configuration and detection algorithm in the context of planetary imaging datasets and retrieved thermal fields. This method is very useful if one has confidence in their manually-detected vortices and wants to apply them as a training set to a larger time series of similar data (observational data, retrievals, or model outputs).

The most glaring issue with the ANN method is that it massively over-estimates the number of vortices with respect to the other two methods. While many of the detected vortices were well-captured on inspection, this method clearly detects many more vorticity features that escaped the human eye and the dynamical constraints of AMEDA. The architecture performs well with respect to performance metrics, so it could be that the ANN vortices were simply weak enough to fall within the visual uncertainties of the manual method (evident in the ANN distribution of vortex intensity), or it was difficult to satisfy the spatial or dynamical constraints of AMEDA for these vortices. We emphasis that this neural network approach is a proof-of-concept and despite this positive early implementation, there is still work to be done in growing the training set and improving the architecture for vortex detection.

Unlike the other two methods, the dynamical approach using AMEDA is "intelligent" – it requires some physical assumptions but applies physical equations directly with the dynamical fields to extract the physical and dynamical properties of vortices. Developed for terrestrial oceanography, it robustly captures the centres and boundaries of eddies and vortices, but is strongly sensitive to the assumptions of Rossby deformation radius and struggles in strongly-disrupted regions. Although this method cannot be used for imaging observations like the others, it does have potential use with thermal retrievals and it is excellent for analysing modelled dynamical fields of any temporal cadence, can be used in global or regional applications, and can be adapted for other planetary bodies. The Okubo–Weiss parameter and the dynamical terms that comprise it have proven to be a very helpful diagnostic tool in understanding and separating the dynamical behaviour of cyclones and anticyclones in the model fields. Having been applied to dynamical observations of terrestrial oceans and now the modelled Saturn atmosphere, there is a potential use case in giant planets whose horizontal wind field is well-resolved (e.g. through high resolution photometry and cloud-tracking).

Dynamical models like AMEDA show the great opportunity to gain useful insights into atmospheric dynamics in cases when machine learning techniques are not applicable. The machine learning model described here (which is purely data-driven) is in fact a totally different approach to AMEDA. Sophisticated approaches are emerging that combine the benefits of equation-driven models with the computational and statistical benefits of machine learning, so called Physics-Informed Neural Networks (PINNs Raissi et al., 2019; Bihlo and Popovych, 2022; Li et al., 2023; Sharma et al., 2023; Kumar et al., 2024; Verma et al., 2024; Zhou et al., 2024), for atmospheric modelling across many sectors. Future operational monitoring of planetary atmospheres could benefit greatly from such an inter-disciplinary application of these techniques.

Importantly, each method presented here does sometimes give slightly different answers, and occasionally there are large discrepancies that are still unexplained. Sometimes there are features that the eye quite easily determines to be a vortex, but AMEDA does not strictly find a closed streamline about a point of maximum angular momentum that also passes the Rossby-scale filter. Other times AMEDA might quite easily find many features that satisfy this condition, but that the human eye would not readily classify as vortex, if indeed it is perceived at all with the given map contrast. Each method has particular use cases and should be chosen according to the specific requirements of the analysis.

4.2. Agreement with observations

All methods broadly reproduce the observed vortex distributions of previous studies. We do not find any long term variability with seasonal changes in solar insolation or mean atmospheric temperature. Vortices only form at the highest latitude westward jets, where the barotropic instability criterion is frequently violated, suggesting that barotropic instability is a necessary condition for cyclogenesis. There is an overall trend towards smaller and more circular vortices, with a meridional correlation with the Rossby deformation radius, implying mutual geostrophic adjustment of eddy fronts and vortex boundaries.

By comparing spatial structure and internal dynamics we confirm that the largest vortices are more rotation-dominated than smaller vortices, allowing them to be more long-lived and stable (and indeed these vortices are present in all model epochs independent of eddy-burst events). Cyclones are more spatially diverse, often being quite zonally-oblate (like the dark cyclonic circulations observed in the atmospheres of Jupiter and Saturn) while anticyclones are almost always circular (like the bright white spots on Jupiter and Saturn). Anticyclones are far more dynamically diverse, exhibiting greater ranges and magnitudes of edge velocity, vorticity, divergence, and lateral strain, and lying further from the pure shear regime than comparably large cyclones. Anticyclones are the strongest vortices in the model and cyclones are never more than half as intense as the strongest anticyclone, potentially reflecting the fundamental dynamical asymmetry in sign-selection.

4.3. Disagreement with observations

The most important differences between the modelled and observed vortices are in the distributions of vortex location and concentration, size, and intensity. Nearby zonal wind conditions seem to be the main driver of vortical structures in the GCM. The magnitudes of zonal wind affect the internal and edge dynamics of the vortices, and the shape of the zonal wind profile affects their formation rate and size.

The non-detection of vortices below $\pm 60°$ latitude could reflect the decreased spatial resolution of the model at low and mid latitudes, but is more likely to be due to the perennial barotropic stability of the flow at these latitudes. Larger zonal jet spacing results in larger shear zones which can produce vortices that are much larger than in observations (even if the overall size trends are similar). In addition,

even with the inherent asymmetric sign selection, a cyclonic bias in concentration remains due to the cyclonic shear zones in the model being simply larger than anticyclonic shear zones. A more realistic jet structure (smaller jet spacing, more jets, less barotropic stability) would likely produce vortices that resemble more closely observations. Finally, the model lacks moist convection which can modify vortices in terms of spatial structure and dynamical behaviour (O'Neill et al., 2015), but also their very formation (because we showed that jet structure influence vortices).

4.4. Future work

The DYNAMICO model often exhibits features and characteristics of all the giant planets at different times. This could point to fundamental differences in dynamical regimes in the atmospheres of the giant planets. A particularly interesting experiment will be to investigate how the planetary Burger number of Brueshaber et al. (2019) correlates to the configuration of the polar vortices as a function of time. The potential implications are that the giant planets themselves may go through their own periods of variability in Burger number and polar vortex configuration, and the DYNAMICO GCM will be valuable tool to further explore this connection.

A quantitative exploration of vortex lifetime and merging/splitting events may provide useful insights into the relationship between the dynamics of the mean flow and the development cycle of large-scale vortices, particularly associated with large-scale eddy-burst events. Identifying the important dynamical drivers of vortex generation and dissipation on the synoptic scale in comparison to observations would reveal the dynamical mechanisms that are well-captured in the model and could highlight areas of further study of GCM vortices.

The conclusions of Boissinot et al. (2024) suggest that moist convection is required to produce a more realistic jet structure and O'Neill et al. (2015) suggest the release of latent heat during moist convection is crucial for accurately representing cyclogenesis. When combined with the conclusions of this work, we raise the question of whether moist convection is required directly to produce more realistic vortices. We speculate here that these vortex distributions may be only indirectly linked to GCM configuration (moist convection, model depth, vertical resolution), such that vortex distributions will be simply as realistic as the zonal jet structure. These methodologies can be applied to the simulations of Boissinot et al. (2024) that include the resolution of moist convection on an extended vertical grid in multiple moist convection schemes (and their associated zonal jet structures).

CRediT authorship contribution statement

Padraig T. Donnelly: Writing – review & editing, Writing – original draft, Visualization, Methodology, Investigation. **Aymeric Spiga:** Supervision, Funding acquisition, Formal analysis, Data curation, Conceptualization. **Sandrine Guerlet:** Writing – review & editing, Supervision, Formal analysis. **Matt K. James:** Methodology, Investigation, Formal analysis. **Deborah Bardet:** Writing – review & editing, Visualization, Methodology.

Declaration of competing interest

The authors declare that they have no known competing financial interests or personal relationships that could have appeared to influence the work reported in this paper.

Data availability

The data used in this study are fully open and available for public access. All the simulations presented in this paper were carried out on the (now defunct) Occigen cluster hosted at CINES and are stored on the ADASTRA cluster hosted at CINES. This work was granted access to the High-Performance Computing (HPC) resources of CINES under the allocations 2015-017357, 2016-017548, A001-0107548, A003-0107548, and A004-0110391 made by GENCI. Processed data can be provided upon request. All code used for post-processing and generation of figures is available on GitHub at https://github.com/PTDonnelly/dynamico_gcm.

Acknowledgements

The authors thank the Editor Julianne Moses and both anonymous reviewers for extremely constructive reviews which helped to improve the manuscript. The authors acknowledge the exceptional computing support from Grand Equipement National de Calcul Intensif (GENCI) and Centre Informatique National de l'Enseignement Supérieur (CINES). All the simulations presented here were carried out on the Occigen cluster hosted at CINES.

Donnelly, Spiga, and Guerlet acknowledge funding from Agence Nationale de la Recherche (ANR), project EMERGIANT ANR-17-CE31-0007, James was supported by Science and Technology Facilities Council (STFC) grant ST/W00089X/1, and Bardet was supported by a European Research Council Consolidator Grant (under the European Union's Horizon 2020 research and innovation program, grant agreement No 723890).

References

Adriani, A., Bracco, A., Grassi, D., Moriconi, M.L., Mura, A., Orton, G., Altieri, F., Ingersoll, A., Atreya, S.K., Lunine, J.I., Migliorini, A., Noschese, R., Cicchetti, A., Sordini, R., Tosi, F., Sindoni, G., Plainaki, C., Dinelli, B.M., Turrini, D., Filacchione, G., Piccioni, G., Bolton, S.J., 2020. Two-year observations of the Jupiter polar regions by JIRAM on board Juno. J. Geophys. Res.: Planets 125, e2019JE006098. http://dx.doi.org/10.1029/2019JE006098.

Adriani, A., Moriconi, M.L., Altieri, F., Sindoni, G., Ingersoll, A.P., Grassi, D., Mura, A., Atreya, S.K., Orton, G., Lunine, J.I., Fletcher, L.N., Simon, A.A., Melin, H., Tosi, F., Cicchetti, A., Noschese, R., Sordini, R., Levin, S., Bolton, J., Plainaki, C., Olivieri, A., 2018. Characterization of Mesoscale Waves in the Jupiter NEB by Jupiter InfraRed Auroral Mapper on board Juno. Astron. J. 156, 246. http://dx.doi.org/10.3847/1538-3881/aae525.

Antuñano, A., Río-Gaztelurrutia, T., Sánchez-Lavega, A., Hueso, R., 2015. Dynamics of Saturn's polar regions. J. Geophys. Res. (Planets) 120, 155–176. http://dx.doi.org/10.1002/2014JE004709.

Antuñano, A., del Río-Gaztelurrutia, T., Sánchez-Lavega, A., Rodríguez-Aseguinolaza, J., 2018. Cloud morphology and dynamics in Saturn's northern polar region. Icarus 299, 117–132. http://dx.doi.org/10.1016/j.icarus.2017.07.017.

Baines, K.H., Momary, T.W., Fletcher, L.N., Showman, A.P., Roos-Serote, M., Brown, R.H., Buratti, B.J., Clark, R.N., Nicholson, P.D., 2009. Saturn's north polar cyclone and hexagon at depth revealed by Cassini/VIMS. Plan. Space Sci. 57, 1671–1681. http://dx.doi.org/10.1016/j.pss.2009.06.026.

Balwada, D., Xiao, Q., Smith, S., Abernathey, R., Gray, A.R., 2021. Vertical fluxes conditioned on vorticity and strain reveal submesoscale ventilation. J. Phys. Oceanogr. 51, 2883–2901. http://dx.doi.org/10.1175/JPO-D-21-0016.1.

Bardet, D., Spiga, A., Guerlet, S., Cabanes, S., Millour, E., Boissinot, A., 2021. Global climate modeling of Saturn's atmosphere. Part IV: Stratospheric equatorial oscillation. Icarus 354, 114042. http://dx.doi.org/10.1016/j.icarus.2020.114042.

Bihlo, A., Popovych, R.O., 2022. Physics-informed neural networks for the shallow-water equations on the sphere. J. Comput. Phys. 456, 111024. http://dx.doi.org/10.1016/j.jcp.2022.111024.

Blake, J.S.D., Fletcher, L.N., Orton, G.S., Antuñano, A., Roman, M.T., Kasaba, Y., Fujiyoshi, T., Melin, H., Bardet, D., Sinclair, J.A., Es-Sayeh, M., 2023. Saturn's seasonal variability from four decades of ground-based mid-infrared observations. Icarus 392, 115347. http://dx.doi.org/10.1016/j.icarus.2022.115347.

Boissinot, A., Spiga, A., Guerlet, S., Cabanes, S., Bardet, D., 2024. Global climate modeling of the Jupiter troposphere and effect of dry and moist convection on jets. Astron. Astrophys. 687, A274. http://dx.doi.org/10.1051/0004-6361/202245220.

Bolton, S.J., Levin, S.M., Guillot, T., Li, C., Kaspi, Y., Orton, G., Wong, M.H., Oyafuso, F., Allison, M., Arballo, J., Atreya, S., Becker, H.N., Bloxham, J., Brown, S.T., Fletcher, L.N., Galanti, E., Gulkis, S., Janssen, M., Ingersoll, A., Lunine, J.L., Misra, S., Steffes, P., Stevenson, D., Waite, J.H., Yadav, R.K., Zhang, Z., 2021. Microwave observations reveal the deep extent and structure of Jupiter's atmospheric vortices. Science 374, 968–972. http://dx.doi.org/10.1126/science.abf1015.

Bouchet, F., Nardini, C., Tangarife, T., 2013. Kinetic theory of jet dynamics in the stochastic barotropic and 2D Navier–Stokes equations. J. Stat. Phys. 153, 572–625. http://dx.doi.org/10.1007/s10955-013-0828-3.

Bouchet, F., Simonnet, E., 2009. Random Changes of Flow Topology in Two-Dimensional and Geophysical Turbulence. Phys. Rev. Lett. 102, 094504. http://dx.doi.org/10.1103/PhysRevLett.102.094504.

Brueshaber, S.R., Sayanagi, K.M., Dowling, T.E., 2019. Dynamical regimes of giant planet polar vortices. Icarus 323, 46–61. http://dx.doi.org/10.1016/j.icarus.2019.02.001.

Cabanes, S., Aurnou, J., Favier, B., Le Bars, M., 2017. A laboratory model for deep-seated jets on the gas giants. Nat. Phys. 13, 387–390. http://dx.doi.org/10.1038/nphys4001.

Cabanes, S., Spiga, A., Young, R.M.B., 2020. Global climate modeling of saturn's atmosphere. Part III: Global statistical picture of zonostrophic turbulence in high-resolution 3d-turbulent simulations. Icarus 345, 113705. http://dx.doi.org/10.1016/j.icarus.2020.113705.

Caldwell, J., Hua, X.M., Turgeon, B., Westphal, J.A., Barnet, C.D., 1993. The drift of Saturn's north polar spot observed by the Hubble Space Telescope. Science 260, 326–329. http://dx.doi.org/10.1126/science.260.5106.326.

Chaigneau, A., Gizolme, A., Grados, C., 2008. Mesoscale eddies off Peru in altimeter records: Identification algorithms and eddy spatio-temporal patterns. Prog. Oceanogr. 79, 106–119. http://dx.doi.org/10.1016/j.pocean.2008.10.013.

Chelton, D.B., Schlax, M.G., Samelson, R.M., de Szoeke, R.A., 2007. Global observations of large oceanic eddies. Geophys. Res. Lett. 34 (L15606), http://dx.doi.org/10.1029/2007GL030812.

de Pater, I., Sromovsky, L.A., Fry, P.M., Hammel, H.B., Baranec, C., Sayanagi, K.M., 2015. Record-breaking storm activity on Uranus in 2014. Icarus 252, 121–128. http://dx.doi.org/10.1016/j.icarus.2014.12.037.

del Genio, A.D., Achterberg, R.K., Baines, K.H., Flasar, F.M., Read, P.L., Sánchez-Lavega, A., Showman, A.P., 2009. Saturn atmospheric structure and dynamics. In: Saturn from Cassini-Huygens. Vol. 11, Springer, pp. 3–159. http://dx.doi.org/10.1007/978-1-4020-9217-6_6, chapter 6.

del Río-Gaztelurrutia, T., Legarreta, J., Hueso, R., Pérez-Hoyos, S., Sánchez-Lavega, A., 2010. A long-lived cyclone in Saturn's atmosphere: Observations and models. Icarus 209, 665–681. http://dx.doi.org/10.1016/j.icarus.2010.04.002.

del Río-Gaztelurrutia, T., Sánchez-Lavega, A., Antuñano, A., Legarreta, J., García-Melendo, E., Sayanagi, K.M., Hueso, R., Wong, M.H., Pérez-Hoyos, S., Rojas, J.F., Simon, A.A., de Pater, I., Blalock, J., Barry, T., 2018. A planetary-scale disturbance in a long living three vortex coupled system in Saturn's atmosphere. Icarus 302, 499–513. http://dx.doi.org/10.1016/j.icarus.2017.11.029.

Dowling, T.E., Ingersoll, A.P., 1989. Jupiter's Great Red Spot as a shallow water system. J. Atmos. Sci. 46, 3256–3278. http://dx.doi.org/10.1175/1520-0469(1989)046<3256:JGRSAA>2.0.CO;2.

Dyudina, U.A., Ingersoll, A.P., Ewald, S.P., Vasavada, A.R., West, R.A., Baines, K.H., Momary, T.W., Del Genio, A.D., Barbara, J.M., Porco, C.C., Achterberg, R.K., Flasar, F.M., Simon-Miller, A.A., Fletcher, L.N., 2009. Saturn's south polar vortex compared to other large vortices in the Solar System. Icarus 202, 240–248. http://dx.doi.org/10.1016/j.icarus.2009.02.014.

Dyudina, U.A., Ingersoll, A.P., Ewald, S.P., Vasavada, A.R., West, R.A., Del Genio, A.D., Barbara, J.M., Porco, C.C., Achterberg, R.K., Flasar, F.M., Simon-Miller, A.A., Fletcher, L.N., 2008. Dynamics of Saturn's south polar vortex. Science 319 (1801), http://dx.doi.org/10.1126/science.1153633.

Flament, P.J., Kennan, S.C., Knox, R.A., Niiler, P.P., Bernstein, R.L., 1996. The three-dimensional structure of an upper ocean vortex in the tropical pacific ocean. Nature 383, 610–613. http://dx.doi.org/10.1038/383610a0.

Fletcher, L.N., de Pater, I., Orton, G.S., Hammel, H.B., Sitko, M.L., Irwin, P.G.J., 2014. Neptune at summer solstice: Zonal mean temperatures from ground-based observations, 2003–2007. Icarus 231, 146–167. http://dx.doi.org/10.1016/j.icarus.2013.11.035.

Fletcher, L.N., Irwin, P.G.J., Orton, G.S., Teanby, N.A., Achterberg, R.K., Bjoraker, G.L., Read, P.L., Simon-Miller, A.A., Howett, C., Kok, R.de., Bowles, N., Calcutt, S.B., Hesman, B., Flasar, F.M., 2008. Temperature and composition of Saturn's polar hot spots and hexagon. Science 319, 79–81. http://dx.doi.org/10.1126/science.1149514.

Fletcher, L.N., King, O.R.T., Harkett, J., Hammel, H.B., Roman, M.T., Melin, H., Hedman, M.M., Moses, J.I., Guerlet, S., Milam, S.N., Tiscareno, M.S., 2023. Saturn's atmosphere in northern summer revealed by jwst/miri. J. Geophys. Res.: Planets 128, e2023JE007924. http://dx.doi.org/10.1029/2023JE007924, arXiv:https://agupubs.onlinelibrary.wiley.com/doi/pdf/10.1029/2023JE007924. e2023JE007924 2023JE007924.

Fletcher, L., Orton, G., Oyafuso, F., Zhang, Z., Brueshaber, S., Wong, M.H., Li, C., Mura, A., Grassi, D., Melin, H., Levin, S., Bolton, S., Rogers, J., Brown, S., 2022. Juno characterisation of cyclonic Folded Filamentary Regions within Jupiter's north polar domain. In: 44th COSPAR Scientific Assembly. Held 16-24 July. p. 536.

Fletcher, L.N., Orton, G.S., Rogers, J.H., Giles, R.S., Payne, A.V., Irwin, P.G.J., Vedovato, M., 2017a. Moist convection and the 2010–2011 revival of Jupiter's South Equatorial Belt. Icarus 286, 94–117. http://dx.doi.org/10.1016/j.icarus.2017.01.001.

Fletcher, L.N., Orton, G.S., Rogers, J.H., Simon-Miller, A.A., de Pater, I., Wong, M.H., Mousis, O., Irwin, P.G.J., Jacquesson, M., Yanamandra-Fisher, P.A., 2011. Jovian temperature and cloud variability during the 2009–2010 fade of the South Equatorial Belt. Icarus 213, 564–580. http://dx.doi.org/10.1016/j.icarus.2011.03.007.

Fletcher, L.N., Orton, G.S., Sinclair, J.A., Donnelly, P., Melin, H., Rogers, J.H., Greathouse, T.K., Kasaba, Y., Fujiyoshi, T., Sato, T.M., Fernandes, J., Irwin, P.G.J., Giles, R.S., Simon, A.A., Wong, M.H., Vedovato, M., 2017b. Jupiter's North Equatorial Belt expansion and thermal wave activity ahead of Juno's arrival. Geophys. Res. Lett. 44, 7140–7148. http://dx.doi.org/10.1002/2017GL073383.

Fletcher, L.N., Orton, G.S., Yanamandra-Fisher, P., Fisher, B.M., Parrish, P.D., Irwin, P.G.J., 2009. Retrievals of atmospheric variables on the gas giants from ground-based mid-infrared imaging. Icarus 200, 154–175. http://dx.doi.org/10.1016/j.icarus.2008.11.019.

Galanti, E., Kaspi, Y., Miguel, Y., Guillot, T., Durante, D., Racioppa, P., Iess, L., 2019. Saturn's deep atmospheric flows revealed by the cassini grand finale gravity measurements. Geophys. Res. Lett. 46, 616–624. http://dx.doi.org/10.1029/2018GL078087.

García-Melendo, E., Sánchez-Lavega, A., Hueso, R., 2007. Numerical models of Saturn's long-lived anticyclones. Icarus 191, 665–677. http://dx.doi.org/10.1016/j.icarus.2007.05.020.

García-Melendo, E., Sánchez-Lavega, A., Legarreta, J., Perez-Hoyos, S., Hueso, R., 2010. A strong high altitude narrow jet detected at Saturn's equator. Geophys. Res. Lett. 37 (L22204), http://dx.doi.org/10.1029/2010GL045434.

Gastine, T., Wicht, J., Duarte, L.D.V., Heimpel, M., Becker, A., 2014. Explaining Jupiter's magnetic field and equatorial jet dynamics. Geophys. Res. Lett. 41, 5410–5419. http://dx.doi.org/10.1002/2014GL060814.

Grassi, D., Adriani, A., Moriconi, M.L., Mura, A., Tabataba-Vakili, F., Ingersoll, A., Orton, G., Hansen, C., Altieri, F., Filacchione, G., Sindoni, G., Dinelli, B.M., Fabiano, F., Bolton, S.J., Levin, S., Atreya, S.K., Lunine, J.I., Momary, T., Tosi, F., Migliorini, A., Piccioni, G., Noschese, R., Cicchetti, A., Plainaki, C., Olivieri, A., Turrini, D., Stefani, S., Sordini, R., Amoroso, M., 2018. First estimate of wind fields in the Jupiter Polar Regions from JIRAM-Juno images. J. Geophys. Res.: Planets 123, 1511–1524. http://dx.doi.org/10.1029/2018JE005555.

Guerlet, S., Spiga, A., Sylvestre, M., Indurain, M., Fouchet, T., Leconte, J., Millour, E., Wordsworth, R., Capderou, M., Bézard, B., Forget, F., 2014. Global climate modeling of Saturn's atmosphere. Part I: Evaluation of the radiative transfer model. Icarus 238, 110–124. http://dx.doi.org/10.1016/j.icarus.2014.05.010.

Guillot, T., Miguel, Y., Militzer, B., Hubbard, W.B., Kaspi, Y., Galanti, E., Cao, H., Helled, R., Wahl, S.M., Iess, L., Folkner, W.M., Stevenson, D.J., Lunine, J.I., Reese, D.R., Biekman, A., Parisi, M., Durante, D., Connerney, J.E.P., Levin, S.M., Bolton, S.J., 2018. A suppression of differential rotation in Jupiter's deep interior. Nature 555, 227–230. http://dx.doi.org/10.1038/nature25775.

Hanel, R., Conrath, B., Flasar, F.M., Kunde, V., Maguire, W., Pearl, J., Pirraglia, J., Samuelson, R., Cruikshank, D., Gautier, D., Gierasch, P., Horn, L., Ponnamperuma, C., 1982. Infrared observations of the Saturnian system from Voyager 2. Science 215, 544–548. http://dx.doi.org/10.1126/science.215.4532.544.

Hanel, R., Conrath, B., Flasar, F.M., Kunde, V., Maguire, W., Pearl, J.C., Pirraglia, J., Samuelson, R., Herath, L., Allison, M., Cruikshank, D.P., Gautier, D., Gierasch, P.J., Horn, L., Koppany, R., Ponnamperuma, C., 1981. Infrared observations of the Saturnian system from Voyager 1. Science 212, 192–200. http://dx.doi.org/10.1126/science.212.4491.192.

Heimpel, M., Aurnou, J., Wicht, J., 2005. Simulation of equatorial and high-latitude jets on Jupiter in a deep convection model. Nature 438, 193–196. http://dx.doi.org/10.1038/nature04208.

Heimpel, M., Gastine, T., Wicht, J., 2016. Simulation of deep-seated zonal jets and shallow vortices in gas giant atmospheres. Nat. Geosci. 9, 19–23. http://dx.doi.org/10.1038/ngeo2601.

Heimpel, M., Gómez Pérez, N., 2011. On the relationship between zonal jets and dynamo action in giant planets. Geophys. Res. Lett. 38 (L14201), http://dx.doi.org/10.1029/2011GL047562.

Holmes, R.M., Thomas, L.N., Thompson, L., Darr, D., 2014. Potential vorticity dynamics of tropical instability vortices. J. Phys. Oceanogr. 44, 995–1011. http://dx.doi.org/10.1175/JPO-D-13-0157.1.

Holton, J., 2004. An Introduction To Dynamic Meteorology. Academic Press.

Hoskins, B.J., Bretherton, F.P., 1972. Atmospheric frontogenesis models: Mathematical formulation and solution. J. Atmos. Sci. 29, 11–37. http://dx.doi.org/10.1175/1520-0469(1972)029<0011:AFMMFA>2.0.CO;2.

Hueso, R., Iñurrigarro, P., Sánchez-Lavega, A., Foster, C.R., Rogers, J.H., Orton, G.S., Hansen, C., Eichstädt, G., Ordonez-Etxeberria, I., Rojas, J.F., Brueshaber, S.R., Sanz-Requena, J.F., Pérez-Hoyos, S., Wong, M.H., Momary, T.W., Jónsson, B., Antuñano, A., Baines, K.H., Dahl, E.K., Mizumoto, S., Go, C., Anguiano-Arteaga, A., 2022. Convective storms in closed cyclones in Jupiter's South Temperate Belt: (I) observations. Icarus 380, 114994. http://dx.doi.org/10.1016/j.icarus.2022.114994.

Ingersoll, A.P., Atreya, S., Bolton, S.J., Brueshaber, S., Fletcher, L.N., Levin, S.M., Li, C., Li, L., Lunine, J.I., Orton, G.S., Waite, H., 2021. Jupiter's overturning circulation: Breaking waves take the place of solid boundaries. Geophys. Res. Lett. 48, e2021GL095756. http://dx.doi.org/10.1029/2021GL095756.

Ingersoll, A.P., Beebe, R.F., Collins, S.A., Hunt, G.E., Mitchell, J.L., Muller, P., Smith, B.A., Terrile, R.J., 1979. Zonal velocity and texture in the jovian atmosphere inferred from Voyager images. Nature 280, 773–775. http://dx.doi.org/10.1038/280773a0.

Ingersoll, A.P., Beebe, R.F., Mitchell, J.L., Garneau, G.W., Yagi, G.M., Muller, J., 1981. Interaction of eddies and mean zonal flow on Jupiter as inferred from Voyager 1 and 2 images. J. Geophys. Res. 86, 8733–8743. http://dx.doi.org/10.1029/JA086iA10p08733.

Ingersoll, A.P., Dowling, T.E., Gierasch, P.J., Orton, G.S., Read, P.L., Sánchez-Lavega, A., Showman, A.P., Simon-Miller, A.A., Vasavada, A.R., 2004. Dynamics of Jupiter's atmosphere. In: Jupiter. the Planet, Satellites and Magnetosphere. pp. 105–128.

Iñurrigarro, P., Hueso, R., Legarreta, J., Sánchez-Lavega, A., Eichstädt, G., Rogers, J.H., Orton, G.S., Hansen, C.J., Pérez-Hoyos, S., Rojas, J.F., Gómez-Forrellad, J.M., 2020. Observations and numerical modelling of a convective disturbance in a large-scale cyclone in Jupiter's South Temperate Belt. Icarus 336, 113475. http://dx.doi.org/10.1016/j.icarus.2019.113475.

Isern-Fontanet, J., García-Ladona, E., Font, J., 2003. Identification of marine eddies from altimetric maps. J. Atmos. Oceanic Technol 20, 772–778. http://dx.doi.org/10.1175/1520-0426(2003)20<772:IOMEFA>2.0.CO;2.

James, M.K., Imber, S.M., Raines, J.M., Yeoman, T.K., Bunce, E.J., 2020. A machine learning approach to classifying MESSENGER FIPS proton spectra. J. Geophys. Res. Space Phys. 125, e2019JA027352. http://dx.doi.org/10.1029/2019JA027352.

Karkoschka, E., Tomasko, M., 2005. Saturn's vertical and latitudinal cloud structure 1991–2004 from HST imaging in 30 filters. Icarus 179, 195–221. http://dx.doi.org/10.1016/j.icarus.2005.05.016.

Karney, C.F.F., 2012. Algorithms for geodesics. J. Geod. 87, 43–55. http://dx.doi.org/10.1007/s00190-012-0578-z.

Kaspi, Y., Flierl, G.R., Showman, A.P., 2009. The deep wind structure of the giant planets: Results from an anelastic general circulation model. Icarus 202, 525–542. http://dx.doi.org/10.1016/j.icarus.2009.03.026.

Kaspi, Y., Galanti, E., Hubbard, W.B., Stevenson, D.J., Bolton, S.J., Iess, L., Guillot, T., Bloxham, J., Connerney, J.E.P., Cao, H., Durante, D., Folkner, W.M., Helled, R., Ingersoll, A.P., Levin, S.M., Lunine, J.I., Miguel, Y., Militzer, B., Parisi, M., Wahl, S.M., 2018. Jupiter's atmospheric jet streams extend thousands of kilometres deep. Nature 555, 223–226. http://dx.doi.org/10.1038/nature25793.

Kumar, P., Vogel, H., Bruckert, J., Muth, L.J., Hoshyaripour, G.A., 2024. Mieai: a neural network for calculating optical properties of internally mixed aerosol in atmospheric models. Npj Clim. Atmos. Sci. 7, 110. http://dx.doi.org/10.1038/s41612-024-00652-y.

Le Vu, B., Stegner, A., Arsouze, T., 2018. Angular Momentum Eddy Detection and Tracking Algorithm (AMEDA) and Its Application to Coastal Eddy Formation. J. Atmos. Ocean. Technol. 35, 739–762. http://dx.doi.org/10.1175/JTECH-D-17-0010.1.

Legarreta, J., Sánchez-Lavega, A., 2005. Jupiter's cyclones and anticyclones vorticity from Voyager and Galileo images. Icarus 174, 178–191. http://dx.doi.org/10.1016/j.icarus.2004.10.006.

Li, B., Hu, Q., Gao, M., Liu, T., Zhang, C., Liu, C., 2023. Physical informed neural network improving the wrf-chem results of air pollution using satellite-based remote sensing data. Atmos. Environ. 311, 120031. http://dx.doi.org/10.1016/j.atmosenv.2023.120031.

Li, C., Ingersoll, A.P., Klipfel, A.P., Brettle, H., 2020. Modeling the stability of polygonal patterns of vortices at the poles of Jupiter as revealed by the Juno spacecraft. Proc. Natl. Acad. Sci. 117, 24082–24087. http://dx.doi.org/10.1073/pnas.2008440117.

Li, L., Ingersoll, A.P., Vasavada, A.R., Porco, C.C., Del Genio, A.D., Ewald, S.P., 2004. Life cycles of spots on Jupiter from Cassini images. Icarus 172, 9–23. http://dx.doi.org/10.1016/j.icarus.2003.10.015.

Li, L., Ingersoll, A.P., Vasavada, A.R., Simon-Miller, A.A., Achterberg, R.K., Ewald, S.P., Dyudina, U.A., Porco, C.C., West, R.A., Flasar, F.M., 2006. Waves in Jupiter's atmosphere observed by the Cassini ISS and CIRS instruments. Icarus 185, 416–429. http://dx.doi.org/10.1016/j.icarus.2006.08.005.

Lian, Y., Showman, A.P., 2008. Deep jets on gas-giant planets. Icarus 194, 597–615. http://dx.doi.org/10.1016/j.icarus.2007.10.014.

Lian, Y., Showman, A.P., 2010. Generation of equatorial jets by large-scale latent heating on the giant planets. Icarus 207, 373–393. http://dx.doi.org/10.1016/j.icarus.2009.10.006.

Limaye, S.S., Sromovsky, L.A., 1991. Winds of Neptune - Voyager observations of cloud motions. J. Geophys. Res. 96 (S01), 18941–18960. http://dx.doi.org/10.1029/91JA01701.

Liu, M., Rossby, T., 1993. Observations of the velocity and vorticity structure of gulf stream meanders. J. Phys. Oceanogr. 23, 329–345. http://dx.doi.org/10.1175/1520-0485(1993)023<0329:OOTVAV>2.0.CO;2.

Liu, J., Schneider, T., 2010. Mechanisms of jet formation on the giant planets. J. Atmos. Sci. 67, 3652–3672. http://dx.doi.org/10.1175/2010JAS3492.1.

Luszcz-Cook, S.H., de Pater, I., Ádámkovics, M., Hammel, H.B., 2010. Seeing double at Neptune's south pole. Icarus 208, 938–944. http://dx.doi.org/10.1016/j.icarus.2010.03.007.

Mac Low, M., Ingersoll, A.P., 1986. Merging of vortices in the atmosphere of Jupiter: An analysis of Voyager images. Icarus 65, 353–369. http://dx.doi.org/10.1016/0019-1035(86)90143-0.

Marcus, P.S., Kundu, T., Lee, C., 2000. Vortex dynamics and zonal flows. Phys. Plasmas 7, 1630–1640. http://dx.doi.org/10.1063/1.874045.

Mitchell, J.L., Terrile, R.J., Smith, B.A., Muller, J.P., Ingersoll, A.P., Hunt, G.E., Collins, S.A., Beebe, R.F., 1979. Jovian cloud structure and velocity fields. Nature 280, 776–778. http://dx.doi.org/10.1038/280776a0.

Mkhinini, N., Coimbra, A., Stegner, A., Arsouze, T., Taupier-Letage, I., Béranger, K., 2014. Long-lived mesoscale eddies in the eastern mediterranean sea: Analysis of 20 years of AVISO geostrophic velocities.. J. Geophys. Res.: Oceans 119, 8603–8626. http://dx.doi.org/10.1002/2014JC010176.

Morales-Juberìas, R., Sánchez-Lavega, A., Lecacheux, J., Colas, F., 2002. A comparative study of jovian cyclonic features from a six-year (1994–2000) survey. Icarus 160, 325–335. http://dx.doi.org/10.1006/icar.2002.6973.

Morrow, R., Birol, F., Griffin, D., Sudre, J., 2004. Divergent pathways of cyclonic and anti-cyclonic ocean eddies. Geophys. Res. Lett. 31 (L24311), http://dx.doi.org/10.1029/2004GL020974.

Niiler, P.P., Maximenko, N.A., Panteleev, G.G., Yamagata, T., Olson, D.B., 2003. Near-surface dynamical structure of the Kuroshio Extension. J. Geophys. Res.: Oceans 108 (3193), http://dx.doi.org/10.1029/2002JC001461.

Okubo, A., 1970. Horizontal dispersion of floatable particles in the vicinity of velocity singularities such as convergences. Deep-Sea Res. Oceanogr. Abstr. 17, 445–454. http://dx.doi.org/10.1016/0011-7471(70)90059-8.

O'Neill, M.E., Emanuel, K.A., Flierl, G.R., 2015. Polar vortex formation in giant-planet atmospheres due to moist convection. Nat. Geosci. 8, 523–526. http://dx.doi.org/10.1038/ngeo2459.

O'Neill, Morgan E, Emanuel, Kerry A., Flierl, Glenn R., 2016. Weak jets and strong cyclones: shallow-water modeling of giant planet polar caps. Journal of the Atmospheric Sciences 73 (4), 1841 – 1855. http://dx.doi.org/10.1175/JAS-D-15-0314.1.

Orton, G.S., Antuñno, L.N., Sinclair, J.A., Momary, T.W., Fujiyoshi, T., Yanamandra-Fisher, P., Donnelly, P.T., Greco, J.J., Payne, A.V., Boydstun, K.A., Wakefield, L.E., 2022. Unexpected long-term variability in Jupiter's tropospheric temperatures. Nat. Astron. 7, 190–197. http://dx.doi.org/10.1038/s41550-022-01839-0.

Orton, G.S., Hansen, C., Caplinger, M., Ravine, M., Atreya, S., Ingersoll, A.P., Jensen, E., Momary, T., Lipkaman, L., Krysak, D., Zimdar, R., Bolton, S., 2017. The first close-up images of Jupiter's polar regions: Results from the Juno mission JunoCam instrument. Geophys. Res. Lett. 44, 4599–4606. http://dx.doi.org/10.1002/2016GL072443.

Orton, G.S., Sinclair, J., Fletcher, L., Fujiyoshi, T., Yanamandra-Fisher, P., Rogers, J., Irwin, P., Greathouse, T., Seede, R., Simon, J., Nguyen, M., Lai, M., 2015. Are brown barges the deserts of the upper jovian atmosphere? In: AAS/Division for Planetary Sciences Meeting Abstracts. p. 502.04.

Orton, G.S., Yanamandra-Fisher, P.A., 2005. Saturn's temperature field from high-resolution middle-infrared imaging. Science 307, 696–698. http://dx.doi.org/10.1126/science.1105730.

Pérez-Hoyos, S., Sánchez-Lavega, A., French, R.G., Rojas, J.F., 2005. Saturn's cloud structure and temporal evolution from ten years of Hubble Space Telescope images (1994–2003). Icarus 176, 155–174. http://dx.doi.org/10.1016/j.icarus.2005.01.014.

Pérez-Hoyos, S., Sanz-Requena, J.F., Barrado-Izagirre, N., Rojas, J.F., Sánchez-Lavega, A., IOPW Team, 2012. The 2009–2010 fade of Jupiter's South Equatorial Belt: Vertical cloud structure models and zonal winds from visible imaging. Icarus 217, 256–271. http://dx.doi.org/10.1016/j.icarus.2011.11.008.

QGIS Development Team, 2022. QGIS Geographic Information System. QGIS Association., URL https://www.qgis.org.

Raissi, M., Perdikaris, P., Karniadakis, G., 2019. Physics-informed neural networks: A deep learning framework for solving forward and inverse problems involving nonlinear partial differential equations. J. Comput. Phys. 378, 686–707. http://dx.doi.org/10.1016/j.jcp.2018.10.045.

Read, P.L., 2011. Dynamics and circulation regimes of terrestrial planets. Plan. Space Sci. 59, 900–914. http://dx.doi.org/10.1016/j.pss.2010.04.024.

Rogers, J., 1995. The Giant Planet Jupiter. Cambridge University Press.

Rogers, J.H., 2007. Jupiter embarks on a 'global upheaval'. J. Br. Astron. Assoc. 117, 113–115.

Rogers, J.H., Mettig, H.J., Adamoli, G., Jacquesson, M., Vedovato, M., 2010. Jupiter in 2010: Interim report: Southern hemisphere. URL http://www.britastro.org/jupiter/2010report08.htm.

Rogers, J.H., Mettig, H.J., Cidadão, A., Clay Sherrod, P., Peach, D., 2006. Merging circulations on Jupiter: Observed differences between cyclonic and anticyclonic mergers. Icarus 185, 244–257. http://dx.doi.org/10.1016/j.icarus.2006.05.022.

Rostami, M., Zeitlin, V., Spiga, A., 2017. On the dynamical nature of Saturn's North Polar hexagon. Icarus 297, 59–70. http://dx.doi.org/10.1016/j.icarus.2017.06.006.

Rothman, L.S., Gordon, I.E., Babikov, Y., Barbe, A., Benner, D.Chris., Bernath, P.F., Birk, M., Bizzocchi, L., Boudon, V., Brown, L.R., Campargue, A., Chance, K., Cohen, E.A., Coudert, L.H., Devi, V.M., Drouin, B.J., Fayt, A., Flaud, J.M., Gamache, R.R., Harrison, J.J., Hartmann, J.M., Hill, C., Hodges, J.T., Jacquemart, D., Jolly, A., Lamouroux, J., Le Roy, R.J., Li, G., Long, D.A., Lyulin, O.M., Mackie, C.J., Massie, S.T., Mikhailenko, S., Müller, H.S.P., Naumenko, O.V.,

Nikitin, A.V., Orphal, J., Perevalov, V., Perrin, A., Polovtseva, E.R., Richard, C., Smith, M.A.H., Starikova, E., Sung, K., Tashkun, S., Tennyson, J., Toon, G.C., Tyuterev, V.G., Wagner, G., 2013. The HITRAN2012 molecular spectroscopic database. J. Quant. Spectro. Rad. Trans. 130, 4–50. http://dx.doi.org/10.1016/j.jqsrt.2013.07.002.

Rudnick, D.L., 2001. On the skewness of vorticity in the upper ocean. Geophys. Res. Lett. 28, 2045–2048. http://dx.doi.org/10.1029/2000GL012265.

Sada, P.V., Beebe, R.F., Conrath, B.J., 1996. Comparison of the structure and dynamics of Jupiter's great red spot between the Voyager 1 and 2 Encounters. Icarus 119, 311–335. http://dx.doi.org/10.1006/icar.1996.0022.

Sánchez-Lavega, A., Hueso, R., Pérez-Hoyos, S., Rojas, J.F., 2006. A strong vortex in Saturn's South Pole. Icarus 184, 524–531. http://dx.doi.org/10.1016/j.icarus.2006.05.020.

Sánchez-Lavega, A., Lecacheux, J., Colas, F., Laques, P., 1993. Ground-based observations of Saturn's North Polar Spot and Hexagon. Science 260, 329–332. http://dx.doi.org/10.1126/science.260.5106.329.

Sánchez-Lavega, A., Rogers, J.H., Orton, G.S., García-Melendo, J., Colas, F., Dauvergne, J.L., Hueso, R., Rojas, J.F., Pérez-Hoyos, S., Mendikoa, I., Iñurrigarro, J.M., Momary, T., Hansen, C.J., Eichstaedt, G., Miles, P., Wesley, A., 2017. A planetary-scale disturbance in the most intense Jovian atmospheric jet from JunoCam and ground-based observations. Geophys. Res. Lett. 44, 4679–4686. http://dx.doi.org/10.1002/2017GL073421.

Sánchez-Lavega, A., Rojas, J.F., Acarreta, J.R., Lecacheux, J., Colas, F., Sada, P.V., 1997. New observations and studies of Saturn's long-lived north polar spot. Icarus 128, 322–334. http://dx.doi.org/10.1006/icar.1997.5761.

Sánchez-Lavega, A., Rojas, J.F., Sada, P.V., 2000. Saturn's zonal winds at cloud level. Icarus 147, 405–420. http://dx.doi.org/10.1006/icar.2000.6449.

Sayanagi, K.M., Blalock, J.J., Dyudina, U.A., Ewald, S.P., Ingersoll, A.P., 2017. Cassini ISS observation of Saturn's north polar vortex and comparison to the south polar vortex. Icarus 285, 68–82. http://dx.doi.org/10.1016/j.icarus.2016.12.011.

Sayanagi, K.M., Dyudina, U.A., Ewald, S.P., Muro, G.D., Ingersoll, A.P., 2014. Cassini ISS observation of Saturn's String of Pearls. Icarus 229, 170–180. http://dx.doi.org/10.1016/j.icarus.2013.10.032.

Scarica, P., Grassi, D., Mura, A., Adriani, A., Ingersoll, A., Li, C., Piccioni, G., Sindoni, G., Moriconi, M.L., Plainaki, C., Altieri, F., Cicchetti, A., Dinelli, B.M., Filacchione, G., Migliorini, A., Noschese, R., Sordini, R., Stefani, S., Tosi, F., Turrini, D., 2022. Stability of the Jupiter southern polar vortices inspected through vorticity using Juno/JIRAM data. J. Geophys. Res.: Planets 127, e2021JE007159. http://dx.doi.org/10.1029/2021JE007159.

Scherbina, A.Y., D'Asaro, E.A., Lee, C.M., Klymak, J.M., Molemaker, M.J., McWilliams, J.C., 2013. Statistics of vertical vorticity, divergence, and strain in a developed submesoscale turbulence field. Geophys. Res. Lett. 40, 4706–4711. http://dx.doi.org/10.1002/grl.50919.

Schneider, T., Liu, J., 2009. Formation of jets and equatorial superrotation on Jupiter. J. Atmos. Sci. 66, 579–601. http://dx.doi.org/10.1175/2008JAS2798.1.

Scott, R.K., 2011. Polar accumulation of cyclonic vorticity. Geophys. Astrophys. Fluid Dyn. 105, 409–420. http://dx.doi.org/10.1080/03091929.2010.509927.

Shakespeare, C.J., 2016. Curved density fronts: Cyclogeostrophic adjustment and frontogenesis. J. Phys. Oceanogr. 46, 3193–3207. http://dx.doi.org/10.1175/JPO-D-16-0137.1.

Sharma, H., Shrivastava, M., Singh, B., 2023. Physics informed deep neural network embedded in a chemical transport model for the amazon rainforest. Npj Clim. Atmos. Sci. 6, 28. http://dx.doi.org/10.1038/s41612-023-00353-y.

Showman, A.P., 2007. Numerical simulations of forced shallow-water turbulence: Effects of moist convection on the large-scale circulation of Jupiter and Saturn. J. Atmos. Sci. 64, 3132–3157. http://dx.doi.org/10.1175/JAS4007.1.

Siegelman, L., Klein, P., Ingersoll, A.P., Ewald, S.P., Young, W.R., Bracco, A., Mura, A., Adriani, A., Grassi, D., Plainaki, C., Sindoni, G., 2022a. Moist convection drives an upscale energy transfer at jovian high latitudes. Nat. Phys. 18, 357–361. http://dx.doi.org/10.1038/s41567-021-01458-y.

Siegelman, L., Young, W.R., Ingersoll, A.P., 2022b. Polar vortex crystals: Emergence and structure. Proc. Natl. Acad. Sci. 119, e2120486119. http://dx.doi.org/10.1073/pnas.2120486119.

Simon-Miller, A.A., Gierasch, P.J., Beebe, R.F., Conrath, B., Flasar, F.M., Achterberg, R.K., the Cassini CIRS Team, 2002. New observational results concerning Jupiter's great red spot. Icarus 158, 249–266. http://dx.doi.org/10.1006/icar.2002.6867.

Smith, B.A., Soderblom, L.A., Banfield, D., Barnet, C., Basilevsky, A.T., Beebe, R.F., Bollinger, K., Boyce, J.M., Brahic, A., Briggs, G.A., Brown, R.H., Chyba, C., Collins, S.A., Colvin, T., Cook, II, .A.F., Crisp, D., Croft, S.K., Cruikshank, D., Cuzzi, J.N., Danielson, G.E., Davies, M.E., Jong, E.De., Dones, L., Godfrey, D., Goguen, J., Grenier, I., Haemmerle, V.R., Hammel, H., Hansen, C.J., Helfenstein, C.P., Howell, C., Hunt, G.E., Ingersoll, A.P., Johnson, T.V., Kargel, J., Kirk, R., Kuehn, D.I., Limaye, S., Masursky, H., McEwen, A., Morrison, D., Owen, T., Owen, W., Pollack, J.B., Porco, C.C., Rages, K., Rogers, P., Rudy, D., Sagan, C., Schwartz, J., Shoemaker, E.M., Showalter, M., Sicardy, B., Simonelli, D., Spencer, J., Sromovsky, L.A., Stoker, C., Strom, R.G., Suomi, V.E., Synott, S.P., Terrile, R.J., Thomas, P., Thompson, W.R., Verbiscer, A., Veverka, J., 1989. Voyager 2 at Neptune - Imaging science results. Science 246, 1422–1449. http://dx.doi.org/10.1126/science.246.4936.1422.

Smith, B.A., Soderblom, L., Batson, R., Bridges, P., Inge, J., Masursky, H., Shoemaker, E., Beebe, R., Boyce, J., Briggs, G., Bunker, A., Collins, S.A., Hansen, C.J., Johnson, T.V., Mitchell, J.L., Terrile, R.J., Cook, II, .A.F., Cuzzi, J., Pollack, J.B., Danielson, G.E., Ingersoll, A.P., Davies, M.E., Hunt, G.E., Morrison, D., Owen, T., Sagan, C., Veverka, J., Strom, R., Suomi, V.E., 1982. A new look at the Saturn system - The Voyager 2 images. Science 215, 504–537. http://dx.doi.org/10.1126/science.215.4532.504.

Smith, B.A., Soderblom, L., Beebe, R.F., Boyce, J.M., Briggs, G., Bunker, A., Collins, S.A., Hansen, C., Johnson, T.V., Mitchell, J.L., Terrile, R.J., Carr, M.H., Cook, A.F., Cuzzi, J.N., Pollack, J.B., Danielson, G.E., Ingersoll, A.P., Davies, M.E., Hunt, G.E., Masursky, H., Shoemaker, E.M., Morrison, D., Owen, T., Sagan, C., Veverka, J., Strom, R., Suomi, V.E., 1981. Encounter with Saturn - Voyager 1 imaging science results. Science 212, 163–191. http://dx.doi.org/10.1126/science.212.4491.163.

Smith, B.A., Soderblom, L.A., Johnson, T.V., Ingersoll, A.P., Collins, S.A., Shoemaker, E.M., Hunt, G.E., Masursky, H., Carr, M.H., Davies, M.E., Cook, A.F., Boyce, J., Danielson, G.E., Owen, T., Sagan, C., Beebe, R.F., Veverka, J., Strom, R.G., McCauley, J.F., Morrison, D., Briggs, G.A., Suomi, V.E., 1979. The Jupiter system through the eyes of Voyager 1. Science 204, 951–957. http://dx.doi.org/10.1126/science.204.4396.951.

Spiga, A., Guerlet, S., Millour, E., Indurain, M., Meurdesoif, Y., Cabanes, S., Dubos, T., Leconte, J., Boissinot, A., Lebonnois, S., Sylvestre, M., Fouchet, T., 2020. Global climate modeling of Saturn's atmosphere. Part II: Multi-annual high-resolution dynamical simulations. Icarus 335, 113377. http://dx.doi.org/10.1016/j.icarus.2019.07.011.

Sromovsky, L.A., Baines, K.H., Fry, P.M., 2018. Models of bright storm clouds and related dark ovals in Saturn's Storm Alley as constrained by 2008 Cassini/VIMS spectra. Icarus 302, 360–385. http://dx.doi.org/10.1016/j.icarus.2017.11.027.

Sromovsky, L.A., Fry, P.M., Hammel, H.B., de Pater, I., Rages, K.A., 2012. Post-equinox dynamics and polar cloud structure on Uranus. Icarus 220, 694–712. http://dx.doi.org/10.1016/j.icarus.2012.05.029.

Sromovsky, L.A., Limaye, S.S., Fry, P.M., 1993. Dynamics of Neptune's major cloud features. Icarus 105, 110–141. http://dx.doi.org/10.1006/icar.1993.1114.

Tabataba-Vakili, F., Rogers, J.H., Eichstädt, G., Orton, G.S., Hansen, C.J., Momary, T.W., Sinclair, J.A., Giles, R.S., Caplinger, M.A., Ravine, M.A., Bolton, S.J., 2020. Long-term tracking of circumpolar cyclones on Jupiter from polar observations with JunoCam. Icarus 335, 113405. http://dx.doi.org/10.1016/j.icarus.2019.113405.

Trammell, H.J., Li, L., Jiang, X., Pan, Y., Smith, M.A., Bering, III, .E.A., Hörst, S.M., Vasavada, A.R., Ingersoll, A.P., Janssen, M.A., West, R.A., Porco, C.C., Li, C., Simon, A.A., Baines, K.H., 2016. Vortices in Saturn's Northern Hemisphere (2008–2015) Observed by Cassini ISS: Vortices in Saturn's NH from Cassini ISS. J. Geophys. Res.: Planets 121, 1814–1826. http://dx.doi.org/10.1002/2016JE005122.

Trammell, H.J., Li, L., Jiang, X., Smith, M., Hörst, S., Vasavada, A., 2014. The global vortex analysis of Jupiter and Saturn based on Cassini Imaging Science Subsystem. Icarus 242, 122–129. http://dx.doi.org/10.1016/j.icarus.2014.07.019.

Vasavada, A.R., Hörst, S.M., Kennedy, M.R., Ingersoll, A.P., Porco, C.C., Del Genio, A.D., West, R.A., 2006. Cassini imaging of Saturn: Southern hemisphere winds and vortices. J. Geophys. Res. 111 (E05004), http://dx.doi.org/10.1029/2005JE002563.

Vasavada, A.R., Ingersoll, A.P., Banfield, D., Bell, M., Gierasch, P.J., Belton, M.J.S., Orton, G.S., Klaasen, K.P., Dejong, E., Breneman, H.H., Jones, T.J., Kaufman, J.M., Magee, K.P., Senske, D.A., 1998. Galileo imaging of Jupiter's atmosphere: The great red spot, equatorial region, and white ovals. Icarus 135, 265–275. http://dx.doi.org/10.1006/icar.1998.5984.

Vasavada, A.R., Showman, A.P., 2005. Jovian atmospheric dynamics: an update after Galileo and Cassini. Rep. Progr. Phys. 68, 1935–1996. http://dx.doi.org/10.1088/0034-4885/68/8/R06.

Verma, Y., Heinonen, M., Garg, V., 2024. ClimODE: Climate and weather forecasting with physics-informed neural ODEs. In: The Twelfth International Conference on Learning Representations. arXiv:2404.10024.

Weiss, J., 1991. The dynamics of enstrophy transfer in two-dimensional hydrodynamics. Phys. D 48, 273–294. http://dx.doi.org/10.1016/0167-2789(91)90088-Q.

Williams, G.P., Yamagata, T., 1984. Geostrophic regimes, intermediate solitary vortices and jovian eddies. J. Atmos. Sci. 41, 453–478. http://dx.doi.org/10.1175/1520-0469(1984)041<0453:GRISVA>2.0.CO;2.

Wong, M.H., Simon, A.A., Tollefson, J.W., de Pater, I., Barnett, M.N., Hsu, A.I., Stephens, A.W., Orton, G.S., Fleming, S.W., Goullaud, C., Januszewski, W., Roman, A., Bjoraker, G.L., Atreya, S.K., Adriani, A., Fletcher, L.N., 2020. High-resolution UV/Optical/IR Imaging of Jupiter in 2016–2019. Astrophys. J. Suppl. Ser. 247, 58. http://dx.doi.org/10.3847/1538-4365/ab775f.

Yano, J.I., Talagrand, O., Drossart, P., 2005. Deep two-dimensional turbulence: An idealized model for atmospheric jets of the giant outer planets. Geophys. Astrophys. Fluid Dyn. 99, 137–150. http://dx.doi.org/10.1080/03091920412331336398.

Zhou, Y., Zhan, R., Wang, Y., Chen, P., Tan, Z., Xie, Z., Nie, X., 2024. A physics-informed deep-learning intensity prediction scheme for tropical cyclones over the Western North Pacific. Adv. Atmos. Sci. 41, 1391–1402. http://dx.doi.org/10.1007/s00376-024-3282-z.